Terahertz-Band Joint Ultra-Massive MIMO Radar-Communications: Model-Based and Model-Free Hybrid Beamforming

Ahmet M. Elbir, *Senior Member IEEE*, Kumar Vijay Mishra, *Senior Member IEEE*, and Symeon Chatzinotas, *Senior Member IEEE*

***Abstract*—Wireless communications and sensing at terahertz (THz) band are increasingly investigated as promising short-range technologies because of the availability of high operational bandwidth at THz. In order to address the extremely high attenuation at THz, ultra-massive multiple-input multiple-output (UM-MIMO) antenna systems have been proposed for THz communications to compensate propagation losses. However, the cost and power associated with fully digital beamformers of these huge antenna arrays are prohibitive. In this paper, we develop THz hybrid beamformers based on both model-based and model-free techniques for a new group-of-subarrays (GoSA) UM-MIMO structure. Further, driven by the recent developments to save the spectrum, we propose beamformers for a joint UM-MIMO radar-communications system, wherein the base station serves multi-antenna user equipment (RX), and tracks radar targets by generating multiple beams toward both RX and the targets. We formulate the GoSA beamformer design as an optimization problem to provide a trade-off between the unconstrained communications beamformers and the desired radar beamformers. Additionally, our design also exploits second-order channel statistics so that an infrequent channel feedback from the RX is achieved with less channel overhead. To further decrease the UM-MIMO computational complexity and enhance robustness, we also implement deep learning solutions to the proposed model-based hybrid beamformers. Numerical experiments demonstrate that both techniques outperform the conventional approaches in terms of spectral efficiency and radar beampatterns, as well as exhibiting less hardware cost and computation time.**

***Index Terms*—Deep learning, hybrid beamforming, joint radar-communications, Terahertz, ultramassive MIMO.**

I. Introduction

In recent years, millimeter-wave (mmWave) spectrum has been extensively studied to address the demands for high data rates in the fifth-generation (5G) wireless communications [1, 2]. The maximum mmWave bandwidth being tens of GHz, it is not possible to achieve data rates of the order of terabits-per-second (Tb/s) without significantly enhancing the current physical-layer efficiency. As a result, the future sixth-generation (6G) networks are expected to exploit the THz frequencies (0.3-10 THz) [3, 4], where hundreds of GHz bandwidth is available to facilitate Tb/s rates without dramatic efficiency increase in the physical-layer [5]. There is, therefore, considerable interest in developing THz wireless solutions [6, 7].

Higher bandwidths also result in improved radar range resolution. At present, mmWave radars with a few GHz bandwidths such as those used in automotive applications [8] at 24 and 77 GHz are unable to yield high-resolution images compared to the optical sensors [9]. Higher operating frequency have smaller antenna apertures and microwave components, which is beneficial for radar deployment on cost and area-sensitive platforms such as drones and ground vehicles. At THz, the physical aperture of the antenna is expected to be very small and the availability of large transmit bandwidth has the potential to offer image resolutions closer to that from the optical sensors [10].

The precise definition of THz band varies among different community members. Recent works in wireless communications generally define this band in the range 0.03-10 THz [11] with an obvious overlap with the conventional mmWave frequencies. For the radar, microwave, and remote sensing engineers, THz band starts at the upper-mmWave limit of 100 GHz and, in particular, *low-THz* term is used for the range 0.1-1 THz [12]. In optics, on the other hand, THz spectrum is defined to end at 10 THz, beyond which frequencies are considered far-infrared [13]. The Terahertz Technology and Applications Committee of the IEEE Microwave Theory and Techniques Society (MTT-S) focuses on 0.3-3 THz range while the IEEE Transactions on Terahertz Science and Technology journal targets 0.3-10 THz. In this paper, in order to be consistent with the developments in THz radar and communications, our work is relevant largely to the low-THz frequencies used by the remote sensing community.

The low-THz spectrum lies in the *atmospheric window* - a region of local minimum attenuation [14, 15]. However, the associated path losses are so high that low-THz radar applications have conventionally been limited to indoor environments such as vital sign monitoring [16], food contamination detection [17], and airport security [18]. Recent characterizations of low-THz radars carried out in the outdoor environments for automotive applications [19, 20] suggest feasibility of operation at a range of up to 200 m with the *specific attenuation* (derivative of attenuation with respect to range) of ~10 dB km^{-1} over 0.1-0.3 THz resulting in a path loss of ~4 dB [21].

For THz communications, high propagation losses and

This work was supported in part by the ERC Project AGNOSTIC.

A. M. E. is with the Department of Electrical and Electronics Engineering, Koç University, Istanbul, Turkey, and SnT, University of Luxembourg, Luxembourg City, Luxembourg (e-mail: ahmetmelbir@gmail.com).

K. V. M. is with the United States Army Research Laboratory, Adelphi, MD 20783 USA (e-mail: kumarvijay-mishra@uiowa.edu).

S. C. is with the SnT at the University of Luxembourg, Luxembourg (e-mail: symeon.chatzinotas@uni.lu).

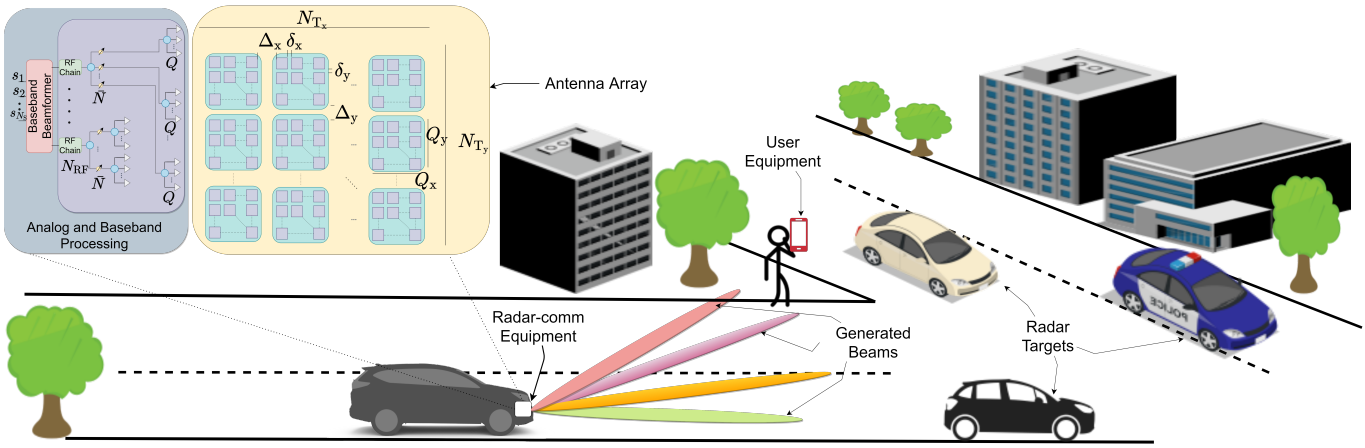

Fig. 1. A radar-communications system for a vehicle-to-vehicle (V2V) and vehicle-to-device (V2D) scenario, wherein a single THz radar-communications unit, with a $N_{\mathrm{T}} = N_{\mathrm{T_x}} \times N_{\mathrm{T_y}}$ antenna array, is mounted onto a vehicle to simultaneously transmit toward both communications receiver and vehicular targets.

power limitations are compensated by the beamforming gains obtained through deployment of extremely dense nano-antenna arrays [22], which may be based on graphene plasmonics [23, 24] or metasurfaces [25]. Analogous to the developments in mmWave communications, [26] proposed a THz ultramassive multiple-input multiple-output (UM-MIMO) architecture that employs an array-of-subarrays (AoSA) of nano-transceivers to increase the coverage and improve the data rates. Various follow-up works (see, e.g., [22] for an overview) showed further UM-MIMO enhancements through waveform design, beamforming, and resource allocation.

With this recent rise of both radar and communications applications at THz, it has been suggested [27] to integrate radar sensing and communications functionalities in future wireless THz systems to facilitate spectrum sharing, enhance pencil beamforming, save hardware cost, and improve resource usage. This follows recent efforts in realizing such *joint radar-communications* (JRC) architectures at mmWave [2], including for *ultrashort ranges* [28], joint MIMO-radar-MIMO-communications [29], and distributed MIMO JRC [30]. In this paper, we focus on a UM-MIMO structure for JRC at THz band.

Analogous to their massive MIMO counterparts at mmWave, the UM-MIMO architecture implies that fully digital beamforming is infeasible because of huge associated cost, area, and power. This necessitates use of hybrid beamforming [31], wherein the signal is processed by both analog and digital beamformer. Although some recent works [32–34] investigate THz hybrid beamformer designs, they do not examine it in the context of the recently proposed, practically feasible UM-MIMO, and more so, its application in THz JRC.

Contrary to prior works, we consider THz hybrid beamforming for a UM-MIMO JRC configuration. To this end, we develop both model-based and model-free techniques that rely on both channel state information (CSI) and channel covariance matrix (CCM). To reduce the hardware complexity, we propose a group of subarrays (GoSAs) structure, in which the antenna elements in the same subarray are connected to the same phase-shifter. Thus, the proposed structure employs even fewer phase-shifters than that of fully-connected (FC) arrays or partially-connected (PC) AoSA structures [35, 36], while providing satisfactory radar and communications performance in terms of the beampattern and the spectral efficiency, respectively. In order to improve the radar performance, the higher degrees of freedom (DoF) are provided by using PC GoSAs. Nevertheless, PC structure has poor spectral efficiency performance compared to the FC array. Hence, we suggest a PC with overlapped (PCO) GoSA structure for performance improvement. To design the hybrid beamformers based on the PCO structure, we propose a modified version of the manifold optimization (MO)-based alternating minimization (AltMin) technique [37], which is originally suggested to solve the beamformer design problem in FC arrays. Our numerical experiments show that the proposed approach has much lower hardware complexity than the state-of-the-art techniques, while maintaining satisfactory radar and communications performance. In this work, our main contributions are:

1) THz UM-MIMO JRC. Our proposed JRC approach based on UM-MIMO is inspired by recent advancements in THz technologies and is, therefore, closer to practical feasibility. It is particularly helpful for short-range vehicular applications, wherein the ego vehicle simultaneously communicates with the user equipment and detect/track the radar targets with higher angular resolution due to high beamforming gain of using ultra-massive number of antennas.

2) Model-based THz hybrid beamforming. Previous research [32–34] examined THz hybrid beamforming without UM-MIMO. Our optimization-based hybrid beamforming for UM-MIMO relies on both CSI and CCM. While the former provides higher spectral efficiency, the latter has lower channel overhead at the cost of slight performance loss.

3) Novel GoSA structure. We propose GoSA structure to lower the hardware cost which could be high for THz systems due to use of a large number of antennas. GoSA allows us to employ fewer number of phase shifters as compared to AoSA. We analyze the performance of GoSA with respect to several design parameters, such as the number of antennas and the antenna spacing. To provide a trade-off between the hardware complexity and the spectral efficiency, PCO-based analog precoder is proposed based on modified MO (MMO) method.

4) Deep learning (DL) solutions. We design two learning models using convolutional neural networks (CNNs), one of which is employed to estimate the direction of the radar targets, whereas the other is used to design the hybrid beamformers. Prior works have not considered learning models for THz JRC hybrid beamformer design.

Throughout this paper, we denote the vectors and matrices by boldface lower and upper case symbols, respectively. In case of a vector $\mathbf{a}$, $[\mathbf{a}]_i$ represents its i-th element. For a matrix $\mathbf{A}$, $[\mathbf{A}]_{i,j}$ denotes the (i,j)-th entry. The $\mathbf{I}_N$ is the identity matrix of size $N \times N$; $\mathbb{E}\{\cdot\}$ denotes the statistical expectation; rank$(\cdot)$ denotes the rank of its matrix argument; $\|\cdot\|_{\mathcal{F}}$ is the Frobenius norm; $(\cdot)^\dagger$ denotes the Moore-Penrose pseudo-inverse; and $\angle\{\cdot\}$ denotes the angle of a complex scalar/vector. The Kronecker and element-wise Hadamard product are denoted by $\otimes$ and $\odot$, respectively. The notation expressing a convolutional layer with N filters/channels of size $D \times D$ is given by $N@D \times D$.

The rest of the paper is organized as follows. In the next section, we describe the system and channel models of GoSA-based UM-MIMO JRC and formulate the beamformer design problem. Section III introduces the CSI- and CCM-based beamformer solutions along with extension to broadband beamfomring. We follow this in Section IV by DL-based solution. We validate our models and methods through numerical experiments in Section V and conclude in Section VI.

II. System Model and Problem Formulation

We consider a UM-MIMO architecture with a JRC system for a vehicle to vehicle (V2V) and vehicle to device (V2D) scenario, in which the transmitter (TX) senses the environment via probing waveforms to the targets and communicates with the receiver (RX), as illustrated in Fig. 1. The antenna arrays at the TX and the RX employ graphene-based plasmonic nano-antennas, which are placed on a metallic surface layer, with a dielectric layer between them [26, 35, 36]. The antennas form a groups of subarrays (GoSAs) structure as each subarray consists of $Q_{\mathrm{x}} \times Q_{\mathrm{y}}$ uniform rectangular arrays (URAs) with $Q = Q_{\mathrm{x}}Q_{\mathrm{y}}$ antennas, as shown in Fig. 1. Also, there are $N_{\mathrm{T}} = N_{\mathrm{T_x}}N_{\mathrm{T_y}}$ and $N_{\mathrm{R}} = N_{\mathrm{R_x}}N_{\mathrm{R_y}}$ subarrays of size Q at the TX and RX, respectively, which form an $N_{\mathrm{T}}Q \times N_{\mathrm{R}}Q$ UM-MIMO transceiver architecture. In each $Q_{\mathrm{x}} \times Q_{\mathrm{y}}$ subarray, the antenna spacing along the x- and y-axis are $\delta_{\mathrm{x}}, \delta_{\mathrm{y}}$ and the distance between each subarray are $\Delta_{\mathrm{x}}, \Delta_{\mathrm{y}}$, respectively.

In the downlink, the TX with N_{T} subarrays, each of which has Q antenna elements, aims to transmit N_{S} data streams towards the RX in the form of $\mathbf{s} = [s_1, \ldots, s_{N_{\mathrm{S}}}]^{\mathsf{T}}$ by using hybrid analog digital beamformers with N_{RF} RF chains, where $\mathbb{E}\{\mathbf{s}\mathbf{s}^{\mathsf{H}}\} = \mathbf{I}_{N_{\mathrm{S}}}$ and $N_{\mathrm{S}} \leq N_{\mathrm{RF}}$. Due to beamforming at subarray level, each subarray of size Q generates a single beam [26]. This is done by connecting the Q antennas in each subarray to a single phase-shifter to lower the hardware complexity. Thus, the TX first applies an $N_{\mathrm{RF}} \times N_{\mathrm{S}}$ baseband precoder $\mathbf{F}_{\mathrm{BB}}$. Then, the signal is passed through an RF precoder $\mathbf{F}_{\mathrm{RF}} \in \mathbb{C}^{N_{\mathrm{T}} \times N_{\mathrm{RF}}}$ by employing N_{T} phase-shifters, as shown in Fig. 2c. In conventional FC structure (see Fig. 2a), each antenna is connected to N_{RF} RF chains while the AoSA model in Fig. 2b has PC structure and it connects each RF chain to $\bar{N}Q$ antennas in each subarray, where $\bar{N} = \frac{N_{\mathrm{T}}}{N_{\mathrm{RF}}}$ [35]. In this work, we propose a GoSA architecture, as shown in Fig. 2c, in which $N_{\mathrm{T}}Q$ antennas are partitioned into N_{RF} groups, each of which has $\bar{N}Q$ antennas. Also, each group consists of $\bar{N}$ subarrays of size Q. We assume that the antennas in each subarray are fed with the same phase shift to reduce the hardware complexity and power consumption, which is critical in THz systems.

In the proposed GoSA model, the RF precoder has unit-modulus constraints, i.e., $|[\mathbf{F}_{\mathrm{RF}}]_{i,j}| = \frac{1}{\sqrt{N_{\mathrm{T}}}}$ as $i \in \{1, \ldots, N_{\mathrm{T}}\}$ and $j \in \{1, \ldots, N_{\mathrm{RF}}\}$, since $\mathbf{F}_{\mathrm{RF}}$ is constructed by using phase-shifters. Furthermore, we have power constrained $\|\mathbf{F}_{\mathrm{RF}}\mathbf{F}_{\mathrm{BB}}\|_{\mathcal{F}} = N_{\mathrm{S}}$. Thus, the $N_{\mathrm{T}} \times 1$ transmitted signal from the TX is given by $\mathbf{x} = \mathbf{F}_{\mathrm{RF}}\mathbf{F}_{\mathrm{BB}}\mathbf{s}$.

A. Communications Model

Assuming frequency-flat fading single-carrier transmission between the TX and RX [26], the received signal at the RX is given by

$$\mathbf{y} = \sqrt{\rho}\mathbf{H}\mathbf{F}_{\mathrm{RF}}\mathbf{F}_{\mathrm{BB}}\mathbf{s} + \mathbf{n}, \tag{1}$$

where $\mathbf{y} \in \mathbb{C}^{N_{\mathrm{R}}}$ is the output of N_{R} subarrayed antennas at the RX, ρ is the received power and $\mathbf{n} \in \mathbb{C}^{N_{\mathrm{R}}}$ denotes the additive white Gaussian noise (AWGN) vector with $\mathbf{n} \sim \mathcal{CN}(\mathbf{0}, \sigma_n^2\mathbf{I}_{N_{\mathrm{R}}})$. $\mathbf{H} \in \mathbb{C}^{N_{\mathrm{R}} \times N_{\mathrm{T}}}$ denotes the THz channel matrix between the TX and the RX.

The structure of the THz channel matrix $\mathbf{H}$ is dominated by the LoS paths while the non-LoS channel components are small due to large reflection loses, scattering and refraction [26, 35]. Channel modeling at THz-band has been a challenge largely because of lack of realistic measurements. Very recently, measurement campaigns at 140 GHz have been reported [38]. The ray-tracing techniques assume the channel to be sparse and dominated by the LoS component for the graphene nano-transceivers [22]. Other channel models such as the 3GPP model [39, 40] are also popular for THz beamforming. In this work, we adopt the Saleh-Valenzuela (SV) THz channel model channel [26, 41], wherein $\mathbf{H}$ is constructed by the superposition of only LoS paths, i.e.,

$$\mathbf{H} = \gamma \sum_{l=1}^{L} \alpha_l \mathbf{A}_{\mathrm{R}}(\Theta_l)\mathbf{A}_{\mathrm{T}}^{\mathsf{H}}(\Psi_l), \tag{2}$$

where $\gamma = \sqrt{\frac{N_{\mathrm{T}}N_{\mathrm{R}}}{L}}$. $\alpha_l \in \mathbb{C}$ denotes the zero-mean Gaussian complex channel gain with variance $\sigma_{\alpha_l}^2$ corresponding to the lth path. Similarly, $\Theta_l = \{\phi_l, \theta_l\}$ and $\Psi_l = \{\varphi_l, \vartheta_l\}$

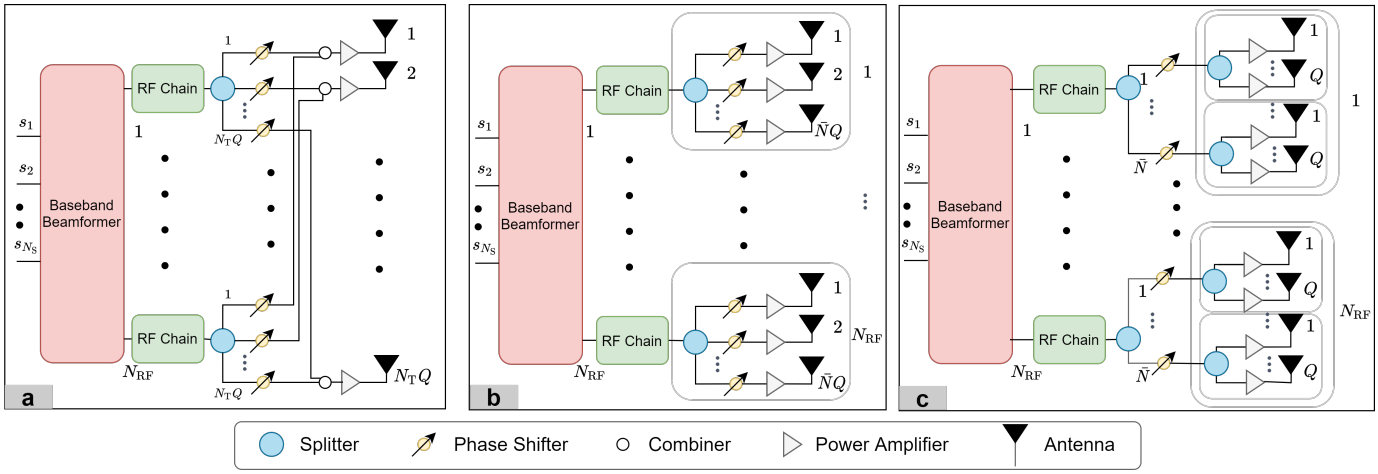

Fig. 2. Hybrid beamforming-based transmitter structures for (a) fully connected, (b) partially-connected array of subarrays (AoSAs) and (c) partially-connected groups of subarrays (GoSAs) architectures. While all the architectures employ $N_{\mathrm{T}}Q$ antennas with N_{RF} RF chains, each antenna is connected to each RF chain via combiners in the fully connected model with $N_{\mathrm{T}}QN_{\mathrm{RF}}$ phase-shifters. In partially-connected AoSA, the same RF chain is connected to $\bar{N}Q$ ($\bar{N}=\frac{N_{\mathrm{T}}}{N_{\mathrm{RF}}}$) antennas with $N_{\mathrm{T}}Q$ phase-shifters totally. In partially-connected GoSA model, each RF chain is connected to $\bar{N}Q$ antennas, introducing N_{T} group of subarrays. There are N_{T} phase-shifters, each of which is connected to Q antennas.

denote the azimuth/elevation angle-of-arrival (AoA) and angle-of-departure (AoD) of the received/transmitted paths at the RX and the TX, respectively. $\mathbf{A}_{\mathrm{R}}(\Theta_l)\in\mathbb{C}^{N_{\mathrm{R}}\times Q}$ and $\mathbf{A}_{\mathrm{T}}(\Psi_l)\in\mathbb{C}^{N_{\mathrm{T}}\times Q}$ are the steering matrices corresponding to the AoAs and AoDs of the GoSAs, respectively, and they are defined as

$$\mathbf{A}_{\mathrm{R}}(\Theta_l)=\begin{bmatrix}\mathbf{a}_{\mathrm{R},1}^{\mathsf{T}}(\Theta_l)\\ \vdots\\ \mathbf{a}_{\mathrm{R},N_{\mathrm{R}}}^{\mathsf{T}}(\Theta_l)\end{bmatrix},\mathbf{A}_{\mathrm{T}}(\Psi_l)=\begin{bmatrix}\mathbf{a}_{\mathrm{T},1}^{\mathsf{T}}(\Psi_l)\\ \vdots\\ \mathbf{a}_{\mathrm{T},N_{\mathrm{T}}}^{\mathsf{T}}(\Psi_l)\end{bmatrix} \tag{3}$$

where $\mathbf{a}_{\mathrm{R},n}(\Theta_l)$ ($\mathbf{a}_{\mathrm{T},m}(\Psi_l)$) is $Q\times 1$ steering vector corresponding to the antennas in the nth (mth) subarray for $n\in\{1\ldots,N_{\mathrm{R}}\}$ ($m\in\{1,\ldots,N_{\mathrm{T}}\}$). The ith element of the transmit steering vector $\mathbf{a}_{\mathrm{T},m}(\Psi_l)$ is given by $[\mathbf{a}_{\mathrm{T},m}(\Psi_l)]_i=\frac{1}{\sqrt{N_{\mathrm{T}}}}\exp\{-\frac{2\pi}{\lambda}\boldsymbol{\kappa}_{m,i}^{\mathsf{T}}\boldsymbol{\Omega}_l\}$, where λ is the wavelength and $\boldsymbol{\kappa}_{m,i}=[x_{m,i},y_{m,i},z_{m,i}]^{\mathsf{T}}$ denotes the position of the ith antenna of the mth subarray in Cartesian coordinate system and $\boldsymbol{\Omega}_l$ is a direction-dependent parameter defined as $\boldsymbol{\Omega}_l=[\cos\varphi_l\sin\vartheta_l,\sin\varphi_l\sin\vartheta_l,\cos\vartheta_l]^{\mathsf{T}}$. The structure of $\mathbf{a}_{\mathrm{R}}(\Theta_l)$ is similar to that of $\mathbf{a}_{\mathrm{T}}(\Psi_l)$. Without loss of generality, we assume that the antennas are perfectly calibrated against mutual coupling and gain/phase mismatches [26]. Then, the (n,m)th element of $\mathbf{H}$ is given by

$$[\mathbf{H}]_{n,m}=\gamma\sum_{l=1}^{L}\alpha_l\mathbf{a}_{\mathrm{R},n}(\Theta_l)\odot\mathbf{a}_{\mathrm{T},m}^{*}(\Psi_l). \tag{4}$$

By connecting the Q antennas in the subarrays to a single phase-shifter, we are able to construct an $N_{\mathrm{T}}\times N_{\mathrm{RF}}$, (instead of $N_{\mathrm{T}}Q\times N_{\mathrm{RF}}$ as in Fig. 2a and Fig. 2b) RF precoder, as illustrated in Fig. 2c. Using partially-connected GoSA, the associated RF precoder has the form of

$$\mathbf{F}_{\mathrm{RF}}=\begin{bmatrix}\mathbf{u}_1 & \mathbf{0} & \cdots & \mathbf{0}\\ \mathbf{0} & \mathbf{u}_2 & \cdots & \mathbf{0}\\ \vdots & \mathbf{0} & \ddots & \mathbf{0}\\ \mathbf{0} & \mathbf{0} & \cdots & \mathbf{u}_{N_{\mathrm{RF}}}\end{bmatrix}\in\mathbb{C}^{N_{\mathrm{T}}\times N_{\mathrm{RF}}}, \tag{5}$$

where $\mathbf{u}_i\in\mathbb{C}^{\bar{N}}$ represents a portion $N_{\mathrm{T}}\times 1$ phase-shifter values with indices $\{(i-1)\bar{N}+1,\ldots,i\bar{N}\}$ for $i\in\{1,\ldots,N_{\mathrm{RF}}\}$, where $\bar{N}=\frac{N_{\mathrm{T}}}{N_{\mathrm{RF}}}$. Each entry of $\mathbf{u}_i$ is then applied to Q antennas in N_{T} subarrays to steer the transmitted beams (see, e.g., Fig. 2c) so that a total of $N_{\mathrm{T}}Q$ antennas are fed.

To address the performance degradation due to GoSA, the columns of $\mathbf{F}_{\mathrm{RF}}$ is designed with overlapping terms [42, 43]. Assume $\bar{\mathbf{u}}_i\in\mathbb{C}^{\bar{M}}$ to include the overlapped phase-shifter terms, where $\bar{M}\in[\bar{N},N_{\mathrm{T}}-N_{\mathrm{RF}}+1]$, for which $\bar{M}=\bar{N}$ provides non-overlapped PC structure as in (5) while $\bar{M}=N_{\mathrm{T}}-N_{\mathrm{RF}}+1$ provides maximum overlap among the phase-shifters. In this case, the performance improvement is at the cost of using more phase-shifters. Nevertheless, it still has lower number of phase-shifters as compared to the partially non-overlapped case in conventional AoSA (see, e.g., Fig. 4). The use of PC/PCO GoSA structure provides higher DoF as compared to the simple phased-array MIMO radar structure, for which $N_{\mathrm{RF}}=1$ [42] and we have a fully-connected MIMO structure when $N_{\mathrm{RF}}=N_{\mathrm{T}}$. While MIMO radar outperforms the phased-array in terms of angular resolution and DoF for parameter estimation and parameter identification, phase-array provides higher coherent processing gain and lower computation and hardware complexity [44]. This complexity is further reduced by using the GoSA structure by feeding each of Q antennas with the same phase shift. Thus, the partially-connected GoSA provides a trade-off between the DoF and the hardware complexity, both of which increase as $N_{\mathrm{RF}}\to N_{\mathrm{T}}$.

In communications-only systems, the aim is to design the hybrid precoders such that the spectral efficiency at the TX is maximized [1, 37, 45], while there are also other related performance metrics, such as energy-efficiency [46] and minimum mean-squared-error (MMSE) [47]. By decoupling the beamformer design problem at the TX and the RX, the mutual information at the TX is maximized instead of spectral efficiency, for which a perfect combiner is assumed

at the receiver [1]. Once the transmitter is designed, the receive beamforming design is done by using the MMSE as performance metric as in [1, 37, 45]. Then the mutual information of the communications system is given by

$$\mathcal{I}(\mathbf{F}_{\mathrm{RF}},\mathbf{F}_{\mathrm{BB}})=\log_2\left|\mathbf{I}_{N_{\mathrm{R}}}+\frac{\rho}{N_{\mathrm{S}}\sigma_n^2}\mathbf{H}\mathbf{F}_{\mathrm{RF}}\mathbf{F}_{\mathrm{BB}}\mathbf{F}_{\mathrm{BB}}^{\mathsf{H}}\mathbf{F}_{\mathrm{RF}}^{\mathsf{H}}\mathbf{H}^{\mathsf{H}}\right|. \tag{6}$$

We note here that the maximization of (6) is provided by exploiting the similarity between the hybrid beamformer $\mathbf{F}_{\mathrm{RF}}\mathbf{F}_{\mathrm{BB}}$ and the optimal unconstrained beamformer $\mathbf{F}_{\mathrm{C}}\in\mathbb{C}^{N_{\mathrm{T}}\times N_{\mathrm{S}}}$. The latter is obtained from the right singular matrix of the channel matrix $\mathbf{H}$ [1, 37]. The singular value decomposition of the channel matrix is $\mathbf{H}=\mathbf{U}_{\mathbf{H}}\mathbf{\Pi}\mathbf{V}_{\mathbf{H}}^{\mathsf{H}}$, where $\mathbf{U}_{\mathbf{H}}\in\mathbb{C}^{N_{\mathrm{R}}\times\mathrm{rank}(\mathbf{H})}$ and $\mathbf{V}_{\mathbf{H}}\in\mathbb{C}^{N_{\mathrm{T}}\times\mathrm{rank}(\mathbf{H})}$ are the left and the right singular value matrices of the channel matrix, respectively, and $\mathbf{\Pi}$ is $\mathrm{rank}(\mathbf{H})\times\mathrm{rank}(\mathbf{H})$ matrix composed of the singular values of $\mathbf{H}$ in descending order. By decomposing $\mathbf{\Pi}$ and $\mathbf{V}_{\mathbf{H}}$ as $\mathbf{\Pi}=\mathrm{diag}\{\widetilde{\mathbf{\Pi}},\overline{\mathbf{\Pi}}\}$, $\mathbf{V}_{\mathbf{H}}=[\widetilde{\mathbf{V}}_{\mathbf{H}},\overline{\mathbf{V}}_{\mathbf{H}}]$, where $\widetilde{\mathbf{V}}_{\mathbf{H}}\in\mathbb{C}^{N_{\mathrm{T}}\times N_{\mathrm{S}}}$, the unconstrained precoder is readily obtained as $\mathbf{F}_{\mathrm{C}}=\widetilde{\mathbf{V}}_{\mathbf{H}}$ [1]. Then, the maximization of (6) is achieved by minimizing the Euclidean distance between $\mathbf{F}_{\mathrm{C}}$ and $\mathbf{F}_{\mathrm{RF}}\mathbf{F}_{\mathrm{BB}}$ as

$$\begin{aligned}\min_{\mathbf{F}_{\mathrm{RF}},\mathbf{F}_{\mathrm{BB}}}\ &\|\mathbf{F}_{\mathrm{RF}}\mathbf{F}_{\mathrm{BB}}-\mathbf{F}_{\mathrm{C}}\|_{\mathcal{F}}\\ \text{s. t.:}\ &\|\mathbf{F}_{\mathrm{RF}}\mathbf{F}_{\mathrm{BB}}\|_{\mathcal{F}}=N_{\mathrm{S}},\\ &|[\mathbf{F}_{\mathrm{RF}}]_{i,j}|=\frac{1}{\sqrt{N_{\mathrm{T}}}},\ \forall i,j.\end{aligned} \tag{7}$$

B. Radar Model

The goal of radar processing is to achieve the highest possible SNR gain towards the direction of interest. The radar first transmits an omni-directional waveforms to detect the unknown targets within the angular space of interest in the search phase, then it generates directional beams towards to the targets for tracking purposes [44]. We assume a subarrayed MIMO radar architecture with GoSAs, wherein each GoSA is used to coherently transmit waveforms that are orthogonal to the ones generated by other GoSAs [42], thereby, coherent processing gain is achieved. To this end, the transmit waveform of the kth GoSA ($k\in\{1,\ldots,K\}$) is designed as $w_k(t)=W(t)e^{j2\pi k\Delta_f t}$, $0<t<T_0$, where $W(t)$ is the pulse shape with duration of T_0, so that the orthogonality of $w_k(t)$ is satisfied for a variety of time delays and Doppler shifts if the frequency increment among the GoSA waveforms satisfies $\Delta_f=|f_{k+1}-f_k|\gg 1/T_0$ [42]. Denote $\{\Phi_1,\ldots,\Phi_K\}$ as the set of target directions ($\Phi_k=(\bar{\varphi}_k,\bar{\vartheta}_k)$), then, the $N_{\mathrm{T}}\times K$ GoSA-MIMO radar-only beamformer is modeled as $\mathbf{F}_{\mathrm{R}}=\mathrm{blkdiag}\{\mathbf{v}_1,\ldots,\mathbf{v}_K\}$ similar to (5), where $\mathbf{v}_k\in\mathbb{C}^{\bar{K}}$ denotes the values of the transmit steering vector $\mathbf{a}_{\mathrm{T}}(\Phi_k)\in\mathbb{C}^{N_{\mathrm{T}}}$ with indices $\{(k-1)\bar{K}+1,\ldots,k\bar{K}\}$ for $k=1\ldots,K$ and $\bar{K}=\frac{N_{\mathrm{T}}}{K}$.It is possible to construct $\mathbf{F}_{\mathrm{R}}$ via overlapped GoSA with $\bar{\mathbf{v}}_k\in\mathbb{C}^{N_{\mathrm{T}}-K+1}$ for $k\in\{1,\ldots,K\}$.

The estimation of the target directions $\{\Phi_k\}_{k=1}^K$ is performed in the search phase of the radar. This is achieved via both: model-based methods, such as MUSIC (*mu*ltiple *si*gnal *c*lassification) algorithm [48], and model-free techniques based on DL [49]. In this work, we assume that search operation is completed and the direction information of the targets is acquired prior to the beamformer design. The beampattern of the radar with GoSA structure is

$$B(\tilde{\Phi})=\mathrm{Trace}\{\mathbf{A}_{\mathrm{T}}^{\mathsf{H}}(\tilde{\Phi})\mathbf{R}\mathbf{A}_{\mathrm{T}}(\tilde{\Phi})\}, \tag{8}$$

where $\mathbf{R}\in\mathbb{C}^{N_{\mathrm{T}}\times N_{\mathrm{T}}}$ is the covariance matrix of the transmitted signal, then the design of the radar beampattern is equivalent to the design of the covariance matrix of the radar probing signals subject to the hybrid architecture of the beamformers. In case of a single target scenario, the optimal beamformer is known to be conventional nonadaptive beamformer, i.e., steering vector corresponding to the direction of interest [42]. When there are multiple targets, the covariance matrix of the transmitted signal is utilized. In case of multiple targets in radar-only scenario with hybrid beamforming, we define the covariance matrix of the transmitted signal $\mathbf{x}$ as

$$\begin{aligned}\mathbf{R}&=\mathbb{E}\{\mathbf{x}\mathbf{x}^{\mathsf{H}}\}=\mathbb{E}\{\mathbf{F}_{\mathrm{RF}}\mathbf{F}_{\mathrm{BB}}\mathbf{s}\mathbf{s}^{\mathsf{H}}\mathbf{F}_{\mathrm{BB}}^{\mathsf{H}}\mathbf{F}_{\mathrm{RF}}^{\mathsf{H}}\},\\ &=\mathbf{F}_{\mathrm{RF}}\mathbf{F}_{\mathrm{BB}}\mathbb{E}\{\mathbf{s}\mathbf{s}^{\mathsf{H}}\}\mathbf{F}_{\mathrm{BB}}^{\mathsf{H}}\mathbf{F}_{\mathrm{RF}}^{\mathsf{H}},\\ &=\mathbf{F}_{\mathrm{RF}}\mathbf{F}_{\mathrm{BB}}\mathbf{F}_{\mathrm{BB}}^{\mathsf{H}}\mathbf{F}_{\mathrm{RF}}^{\mathsf{H}},\end{aligned} \tag{9}$$

which requires the design of hybrid beamformers $\mathbf{F}_{\mathrm{RF}}$, $\mathbf{F}_{\mathrm{BB}}$. The hybrid beamformer design problem for radar-only system is solved by minimizing the Euclidean distance between $\mathbf{F}_{\mathrm{RF}}\mathbf{F}_{\mathrm{BB}}$ and $\mathbf{F}_{\mathrm{R}}\mathbf{P}$ as

$$\begin{aligned}\min_{\mathbf{F}_{\mathrm{RF}},\mathbf{F}_{\mathrm{BB}},\mathbf{P}}\ &\|\mathbf{F}_{\mathrm{RF}}\mathbf{F}_{\mathrm{BB}}-\mathbf{F}_{\mathrm{R}}\mathbf{P}\|_{\mathcal{F}}\\ \text{s. t.:}\ &\|\mathbf{F}_{\mathrm{RF}}\mathbf{F}_{\mathrm{BB}}\|_{\mathcal{F}}=N_{\mathrm{S}},\\ &|[\mathbf{F}_{\mathrm{RF}}]_{i,j}|=\frac{1}{\sqrt{N_{\mathrm{T}}}},\ \forall i,j,\\ &\mathbf{P}\mathbf{P}^{\mathsf{H}}=\mathbf{I}_{N_{\mathrm{S}}},\end{aligned} \tag{10}$$

where the unitary matrix $\mathbf{P}\in\mathbb{C}^{K\times N_{\mathrm{S}}}$ is an auxiliary variable to provide a change of dimension between $\mathbf{F}_{\mathrm{RF}}\mathbf{F}_{\mathrm{BB}}$ and $\mathbf{F}_{\mathrm{R}}$ without causing any distortion in the radar beampattern and $\mathbf{P}\mathbf{P}^{\mathsf{H}}=\mathbf{I}_K$.

C. Problem Formulation

The aim of this work is designing the hybrid beamformer $\mathbf{F}_{\mathrm{RF}}\mathbf{F}_{\mathrm{BB}}$ to simultaneously maximize the spectral efficiency of the communications link and provide as much SNR as possible towards the radar targets by forming the beampattern of the transmit antenna array. To jointly solve the problems in (7) and (10), we formulate the following problem,

$$\begin{aligned}\min_{\mathbf{F}_{\mathrm{RF}},\mathbf{F}_{\mathrm{BB}},\mathbf{P}}\ &\eta\|\mathbf{F}_{\mathrm{RF}}\mathbf{F}_{\mathrm{BB}}-\mathbf{F}_{\mathrm{C}}\|_{\mathcal{F}}+(1-\eta)\|\mathbf{F}_{\mathrm{RF}}\mathbf{F}_{\mathrm{BB}}-\mathbf{F}_{\mathrm{R}}\mathbf{P}\|_{\mathcal{F}}\\ \text{s. t.:}\ &\|\mathbf{F}_{\mathrm{RF}}\mathbf{F}_{\mathrm{BB}}\|_{\mathcal{F}}=N_{\mathrm{S}},\\ &|[\mathbf{F}_{\mathrm{RF}}]_{i,j}|=\frac{1}{\sqrt{N_{\mathrm{T}}}},\ \forall i,j\in\mathcal{S},\\ &|[\mathbf{F}_{\mathrm{RF}}]_{i,j}|=0,\ \forall i,j\in\bar{\mathcal{S}},\\ &\mathbf{P}\mathbf{P}^{\mathsf{H}}=\mathbf{I}_{N_{\mathrm{S}}},\end{aligned} \tag{11}$$

where $\mathcal{S}$ and $\bar{\mathcal{S}}$ denotes the set of non-zero and zero terms in $\mathbf{F}_{\mathrm{RF}}$ due to overlapped structure in (5), respectively. In (11), $0\leq\eta\leq 1$ provides the trade-off between the radar

and communications tasks. If $\eta = 1$ ($\eta = 0$), (11) corresponds to communications-only (radar-only) beamformer design problem. The optimization problem (11) is difficult solve because of several matrix variables $\mathbf{F}_{\mathrm{RF}}, \mathbf{F}_{\mathrm{BB}}, \mathbf{P}$, and non-convex constraints. A common approach is to use alternating techniques, i.e., estimating the unknown variables one-by-one while fixing the others. While this approach does not guarantee the optimality, its convergence is proved in the relevant literature, e.g., [37, 45, 50, 51].

Assumption 1: We assume that the channel matrix $\mathbf{H}$ is available for CSI-based beamformer design (see, e.g., Section III-A). If necessary, the estimation of $\mathbf{H}$ is performed via compressed sensing, angle-domain processing or coordinated pilot-assignment [52] techniques. In addition, there exist model-free channel estimation techniques, e.g., [53, 54].

Assumption 2: We assume that the CCM is available at the TX for statistical beamformer design (see, e.g., Section III-B). In practice, the CCM is estimated by several algorithms such as temporal averaging techniques which collect the single snapshot received signal, compressed covariance sensing approaches and power angular spectrum estimation [55] as well as model-based approaches, e.g., [56].

III. Model-Based Hybrid Beamformer Design

In this part, we introduce our model-based hybrid beamformer design techniques relying on the CSI and CCM-based channel information.

A. Hybrid Beamformer Design With CSI

Denote $f(\mathbf{F}_{\mathrm{RF}}, \mathbf{F}_{\mathrm{BB}}, \mathbf{P})$ as the cost function in (11), which is rewritten as

$$f(\mathbf{F}_{\mathrm{RF}}, \mathbf{F}_{\mathrm{BB}}, \mathbf{P}) = \|\eta[\mathbf{F}_{\mathrm{RF}}\mathbf{F}_{\mathrm{BB}} - \mathbf{F}_{\mathrm{C}}]\|_{\mathcal{F}} + \|(1-\eta)[\mathbf{F}_{\mathrm{RF}}\mathbf{F}_{\mathrm{BB}} - \mathbf{F}_{\mathrm{R}}\mathbf{P}]\|_{\mathcal{F}}. \quad (12)$$

Then, using triangle inequality, we get

$$\begin{aligned} f(\mathbf{F}_{\mathrm{RF}}, \mathbf{F}_{\mathrm{BB}}, \mathbf{P}) &\geq \\ &\|\eta\mathbf{F}_{\mathrm{RF}}\mathbf{F}_{\mathrm{BB}} - \eta\mathbf{F}_{\mathrm{C}} + (1-\eta)\mathbf{F}_{\mathrm{RF}}\mathbf{F}_{\mathrm{BB}} - (1-\eta)\mathbf{F}_{\mathrm{R}}\mathbf{P}\|_{\mathcal{F}} \\ &= \|\mathbf{F}_{\mathrm{RF}}\mathbf{F}_{\mathrm{BB}} - \eta\mathbf{F}_{\mathrm{C}} - (1-\eta)\mathbf{F}_{\mathrm{R}}\mathbf{P}\|_{\mathcal{F}}. \end{aligned} \quad (13)$$

Define $\mathbf{F}_{\mathrm{CR}} \in \mathbb{C}^{N_{\mathrm{T}} \times N_{\mathrm{S}}}$ as the JRC beamformer as

$$\mathbf{F}_{\mathrm{CR}} = \eta\mathbf{F}_{\mathrm{C}} + (1-\eta)\mathbf{F}_{\mathrm{R}}\mathbf{P}, \quad (14)$$

and define the new cost function $\bar{f}(\mathbf{F}_{\mathrm{RF}}, \mathbf{F}_{\mathrm{BB}}, \mathbf{P})$ as

$$\bar{f}(\mathbf{F}_{\mathrm{RF}}, \mathbf{F}_{\mathrm{BB}}, \mathbf{P}) = \|\mathbf{F}_{\mathrm{RF}}\mathbf{F}_{\mathrm{BB}} - \mathbf{F}_{\mathrm{CR}}\|_{\mathcal{F}}, \quad (15)$$

where we have $\bar{f}(\mathbf{F}_{\mathrm{RF}}, \mathbf{F}_{\mathrm{BB}}, \mathbf{P}) \leq f(\mathbf{F}_{\mathrm{RF}}, \mathbf{F}_{\mathrm{BB}}, \mathbf{P})$ due to (13). Then, we rewrite the optimization problem (11) in a compact form as

$$\begin{aligned} \min_{\mathbf{F}_{\mathrm{RF}}, \mathbf{F}_{\mathrm{BB}}, \mathbf{P}} \quad & \|\mathbf{F}_{\mathrm{RF}}\mathbf{F}_{\mathrm{BB}} - \mathbf{F}_{\mathrm{CR}}\|_{\mathcal{F}} \\ \text{s. t.:} \quad & \|\mathbf{F}_{\mathrm{RF}}\mathbf{F}_{\mathrm{BB}}\|_{\mathcal{F}} = N_{\mathrm{S}}, && (16a) \\ & |[\mathbf{F}_{\mathrm{RF}}]_{i,j}| = \frac{1}{\sqrt{N_{\mathrm{T}}}}, \ \forall i,j \in \mathcal{S}, && (16b) \\ & |[\mathbf{F}_{\mathrm{RF}}]_{i,j}| = 0, \ \forall i,j \in \bar{\mathcal{S}}, && (16c) \\ & \mathbf{P}\mathbf{P}^{\mathsf{H}} = \mathbf{I}_{N_{\mathrm{S}}}. && (16d) \end{aligned}$$

Now, the problem (16) looks similar to the communications-only problem in (7), and is solved via alternating minimization techniques suggested to solve (7), e.g., [1, 37]. In this case, $\mathbf{F}_{\mathrm{RF}}$, $\mathbf{F}_{\mathrm{BB}}$ and $\mathbf{P}$ are estimated one-by-one while the others are fixed. By fixing $\mathbf{F}_{\mathrm{RF}}$ and $\mathbf{F}_{\mathrm{BB}}$, $\mathbf{P}$ is found via the SVD of the matrix $\mathbf{F}_{\mathrm{R}}^{\mathsf{H}}\mathbf{F}_{\mathrm{RF}}\mathbf{F}_{\mathrm{BB}}$, i.e.,

$$\mathbf{P} = \widetilde{\mathbf{U}}\mathbf{I}_{K \times N_{\mathrm{S}}}\widetilde{\mathbf{V}}, \quad (17)$$

for which we have $\widetilde{\mathbf{U}}\mathbf{\Sigma}\widetilde{\mathbf{V}}^{\mathsf{H}} = \mathbf{F}_{\mathrm{R}}^{\mathsf{H}}\mathbf{F}_{\mathrm{RF}}\mathbf{F}_{\mathrm{BB}}$ and $\mathbf{I}_{K \times N_{\mathrm{S}}} = [\mathbf{I}_K, \mathbf{0}_{K \times (N_{\mathrm{S}}-K)}]$ [1]. Similarly, when $\mathbf{F}_{\mathrm{RF}}$ and $\mathbf{P}$ are fixed, $\mathbf{F}_{\mathrm{BB}}$ is calculated as $\mathbf{F}_{\mathrm{BB}} = \mathbf{F}_{\mathrm{RF}}^{\dagger}\mathbf{F}_{\mathrm{CR}}$, and normalized as $\mathbf{F}_{\mathrm{BB}} = \frac{\sqrt{N_{\mathrm{S}}}}{\|\mathbf{F}_{\mathrm{RF}}\mathbf{F}_{\mathrm{BB}}\|_{\mathcal{F}}}\mathbf{F}_{\mathrm{BB}}$.

The main challenge in (16) is the estimation of $\mathbf{F}_{\mathrm{RF}}$ due to unit-modulus constraints. In FC case, $\mathbf{F}_{\mathrm{RF}}$ is found via MO-based techniques and the optimal solution is readily obtained for PC structure via phase-rotation [37, 51]. However, the design of $\mathbf{F}_{\mathrm{RF}}$ for the overlapped case is not straightforward due to the constraint (16c). Thus, we propose a MMO-based solution to account for (16c) in the following.

Assume that $\mathbf{F}_{\mathrm{BB}}$ and $\mathbf{P}$ are fixed, then (16) is written in vectorized form as

$$\begin{aligned} \min_{\mathbf{f}_{\mathrm{RF}}} \quad & \|\mathbf{G}\mathbf{f}_{\mathrm{RF}} - \mathbf{f}_{\mathrm{CR}}\|_{\mathcal{F}} \\ \text{s. t.:} \quad & |[\mathbf{f}_{\mathrm{RF}}]_i| = \frac{1}{\sqrt{N_{\mathrm{T}}}}, \ \forall i \in \mathcal{V}, \\ & |[\mathbf{f}_{\mathrm{RF}}]_i| = 0, \ \forall i \in \bar{\mathcal{V}}, \end{aligned} \quad (18)$$

where $\mathbf{G} = (\mathbf{F}_{\mathrm{BB}}^{\mathsf{T}}) \otimes \mathbf{I}_{N_{\mathrm{T}}} \in \mathbb{C}^{N_{\mathrm{T}}N_{\mathrm{S}} \times N_{\mathrm{T}}N_{\mathrm{RF}}}$, $\mathbf{f}_{\mathrm{RF}} = \mathrm{vec}\{\mathbf{F}_{\mathrm{RF}}\} \in \mathbb{C}^{N_{\mathrm{T}}N_{\mathrm{RF}}}$ and $\mathbf{f}_{\mathrm{CR}} = \mathrm{vec}\{\mathbf{F}_{\mathrm{CR}}\} \in \mathbb{C}^{N_{\mathrm{T}}N_{\mathrm{S}}}$. $\mathcal{V}$ and $\bar{\mathcal{V}}$ denote the set of non-zero and zero terms in $\mathbf{f}_{\mathrm{RF}}$, respectively. The sizes of $\mathcal{V}$ and $\bar{\mathcal{V}}$ depend on the selection of $\bar{M}$. As an example, for $N_{\mathrm{T}} = 100$, $N_{\mathrm{RF}} = 10$ and $\bar{M} = N_{\mathrm{RF}}(N_{\mathrm{T}} - N_{\mathrm{RF}} + 1)$, we have $|\mathcal{V}| = 910$ and $|\bar{\mathcal{V}}| = 90$. Now, the aim is to exclude the portion of $\mathbf{G}$ and $\mathbf{f}_{\mathrm{RF}}$ corresponding to $\bar{\mathcal{V}}$ and find the portion of $\mathbf{f}_{\mathrm{RF}}$ corresponding to $\mathcal{V}$ so that we employ MO accordingly and all the elements of the unknown vector will obey unit-modulus constraints.

Lemma 1. *Define $\mathbf{G}_{\mathcal{V}} \in \mathbb{C}^{N_{\mathrm{T}}N_{\mathrm{S}} \times T}$ and $\mathbf{f}_{\mathrm{RF}_{\mathcal{V}}} \in \mathbb{C}^{T}$ as the portion of $\mathbf{G}$ and $\mathbf{f}_{\mathrm{RF}}$ corresponding to $\mathcal{V}$, where T is the number of remaining columns (entries) of $\mathbf{G}$ ($\mathbf{f}_{\mathrm{RF}}$) after excluding the terms related to $\bar{\mathcal{V}}$. Then, the optimization problem in (18) is equivalent to*

$$\begin{aligned} \min_{\mathbf{f}_{\mathrm{RF}_{\mathcal{V}}}} \quad & \|\mathbf{G}_{\mathcal{V}}\mathbf{f}_{\mathrm{RF}_{\mathcal{V}}} - \mathbf{f}_{\mathrm{CR}}\|_{\mathcal{F}} \\ \text{s. t.:} \quad & |[\mathbf{f}_{\mathrm{RF}_{\mathcal{V}}}]_i| = \frac{1}{\sqrt{N_{\mathrm{T}}}}, \ \forall i \in \mathcal{V}. \end{aligned} \quad (19)$$

Proof: The cost of problem (18) is

$$\begin{aligned} \|[\mathbf{G}_{\mathcal{V}}, \mathbf{G}_{\bar{\mathcal{V}}}] \begin{bmatrix} \mathbf{f}_{\mathrm{RF}_{\mathcal{V}}} \\ \mathbf{f}_{\mathrm{RF}_{\bar{\mathcal{V}}}} \end{bmatrix} - \mathbf{f}_{\mathrm{CR}}\|_{\mathcal{F}} &= \|\mathbf{G}_{\mathcal{V}}\mathbf{f}_{\mathrm{RF}_{\mathcal{V}}} + \mathbf{G}_{\bar{\mathcal{V}}}\mathbf{f}_{\mathrm{RF}_{\bar{\mathcal{V}}}} - \mathbf{f}_{\mathrm{CR}}\|_{\mathcal{F}} \\ &= \|\mathbf{G}_{\mathcal{V}}\mathbf{f}_{\mathrm{RF}_{\mathcal{V}}} - \mathbf{f}_{\mathrm{CR}}\|_{\mathcal{F}}. \end{aligned} \quad (20)$$

Since $\mathbf{f}_{\mathrm{RF}_{\bar{\mathcal{V}}}} = \mathbf{0}_{N_{\mathrm{T}}N_{\mathrm{RF}}-T} \times 1$, we have $\mathbf{G}_{\bar{\mathcal{V}}}\mathbf{f}_{\mathrm{RF}_{\bar{\mathcal{V}}}} = \mathbf{0}_{N_{\mathrm{T}}N_{\mathrm{S}} \times (N_{\mathrm{T}}N_{\mathrm{RF}}-T)}$, and thus (18) is equivalent to (19). ■

Using Lemma 1, we solve (19) via MO, for which the search space is regarded as a *Riemannian submanifold* $\mathcal{M}$ of

complex plane $\mathbb{C}^T$ since $\mathbf{f}_{\mathrm{RF}_\mathcal{V}} \in \mathbb{C}^T$ forms a complex circle manifold, i.e., $\mathcal{M}_{cc}^T = \{\mathbf{f}_{\mathrm{RF}_\mathcal{V}} \in \mathbb{C}^T : |[\mathbf{f}_{\mathrm{RF}_\mathcal{V}}]_1| = |[\mathbf{f}_{\mathrm{RF}_\mathcal{V}}]_2| = \cdots = |[\mathbf{f}_{\mathrm{RF}_\mathcal{V}}]_T| = \frac{1}{\sqrt{N_\mathrm{T}}}\}$ due to unit-modulus constraint. Define the Riemannian gradient at $\mathbf{f}_{\mathrm{RF}_\mathcal{V}}$, $\mathrm{grad} f(\mathbf{f}_{\mathrm{RF}_\mathcal{V}})$ as the orthogonal projection of the Euclidean gradient $\nabla f(\mathbf{f}_{\mathrm{RF}_\mathcal{V}})$ onto the tangent space of $\mathbf{f}_{\mathrm{RF}_\mathcal{V}}$, i.e.,

$$\mathrm{grad} f(\mathbf{f}_{\mathrm{RF}_\mathcal{V}}) = \nabla f(\mathbf{f}_{\mathrm{RF}_\mathcal{V}}) - \mathrm{Re}\{\nabla f(\mathbf{f}_{\mathrm{RF}_\mathcal{V}}) \odot \mathbf{f}_{\mathrm{RF}_\mathcal{V}}^*\} \odot \mathbf{f}_{\mathrm{RF}_\mathcal{V}},$$

where the Euclidean gradient of the cost function in (19) is given by

$$\nabla f(\mathbf{f}_{\mathrm{RF}_\mathcal{V}}) = -2\mathbf{G}_\mathcal{V}^\mathsf{H}[\mathbf{f}_{\mathrm{CR}} - \mathbf{G}_\mathcal{V}\mathbf{f}_{\mathrm{RF}_\mathcal{V}}]. \tag{21}$$

After defining the cost function and the gradient as in (19) and (21), the remaining part of the solution is similar to the conventional MO algorithm [57]. This is done via the conjugate gradient descent technique iteratively such that $\mathbf{f}_{\mathrm{RF}_\mathcal{V}}^{(k+1)}$ at the kth iteration is obtained with the update rule

$$\mathbf{f}_{\mathrm{RF}_\mathcal{V}}^{(k+1)} = \frac{(\mathbf{f}_{\mathrm{RF}_\mathcal{V}}^{(k)} + \alpha_k \mathbf{d}^{(k)})}{|(\mathbf{f}_{\mathrm{RF}_\mathcal{V}}^{(k)} + \alpha_k \mathbf{f}_{\mathrm{RF}_\mathcal{V}}^{(k)})|}, \tag{22}$$

where α_k is Armijo backtracking line search step size [57] and $\mathbf{d}_k$ denotes the direction of decrease, which is defined as $\mathbf{d}_k = -\mathrm{grad} f(\mathbf{f}_{\mathrm{RF}_\mathcal{V}}^{(k)}) + \beta_k \bar{\mathbf{d}}^{(k-1)}$, for which $\mathrm{grad} f(\mathbf{f}_{\mathrm{RF}_\mathcal{V}}^{(k)})$ denotes the Riemannian gradient at the kth iteration and β_k is the Polak-Ribiere parameter. $\bar{\mathbf{d}}^{(k)}$ is the vector transport of conjugate direction $\mathbf{d}^{(k)}$, which is defined as $\bar{\mathbf{d}}^{(k)} = \mathbf{d}^{(k)} - \mathrm{Re}\{\mathbf{d}^{(k)} \odot \mathbf{f}_{\mathrm{RF}_\mathcal{V}}^{(k+1)}\} \odot \mathbf{f}_{\mathrm{RF}_\mathcal{V}}^{(k+1)}$, where $\mathbf{f}_{\mathrm{RF}_\mathcal{V}}^{(k+1)}$ is directly obtained from (22) and $\mathbf{d}_0 = -\mathrm{grad} f(\mathbf{f}_{\mathrm{RF}_\mathcal{V}}^{(0)})$. The optimization process is initialized from a random point, i.e., $[\mathbf{f}_{\mathrm{RF}_\mathcal{V}}^{(0)}]_t = e^{j\bar{\theta}_t}$ where $\bar{\theta}_t \sim \mathrm{uniform}([0, 2\pi))$, $t = 1, \ldots, T$. Once the non-zero entries of $\mathbf{f}_{\mathrm{RF}}$, i.e., $\mathbf{f}_{\mathrm{RF}_\mathcal{V}}$ is optimized, then RF precoder $\mathbf{F}_{\mathrm{RF}} \in \mathbb{C}^{N_\mathrm{T} \times N_{\mathrm{RF}}}$ is reconstructed from $\mathbf{f}_{\mathrm{RF}_\mathcal{V}}$ according to the index sets $\mathcal{V}$, $\bar{\mathcal{V}}$, $\mathcal{S}$ and $\bar{\mathcal{S}}$.

In (16), the convergence to an optimum solution is guaranteed such that the Euclidean distance between the radar-communications beamformer $\mathbf{F}_{\mathrm{CR}}$ and the hybrid beamformer $\mathbf{F}_{\mathrm{RF}}\mathbf{F}_{\mathrm{BB}}$ is minimized [37]. We present the algorithmic steps of the CSI-based hybrid beamformer design in Algorithm 1. The implementation of the iterative algorithm takes no more than 10 iterations while the MMO steps requires approximately 20 sub-iterations for the settings $N_\mathrm{T} = 1024$, $Q = 9$ and $N_{\mathrm{RF}} = 10$.

The hybrid beamformer design problem in (16) should be solved for every η. Furthermore, $\mathbf{P}$ changes even if $\mathbf{F}_\mathrm{R}$ is kept fixed since it matches the hybrid beamformer to the unconstrained radar-only beamformer. As a special case, where $\mathbf{P} = \mathbf{I}_\mathrm{K}$, i.e., $K = N_\mathrm{S}$, the following lemma shows that the solution of (16) is obtained from the linear combination of the solutions of communications- and radar-only problems in (7) and (10), respectively.

Lemma 2. *Denote $\widetilde{\mathbf{F}}_\mathrm{C} \in \mathbb{C}^{N_\mathrm{T} \times N_\mathrm{S}}$ and $\widetilde{\mathbf{F}}_\mathrm{R} \in \mathbb{C}^{N_\mathrm{T} \times N_\mathrm{S}}$ as the hybrid beamforming solutions of (7) and (10), respectively. Then, the solution of (16) is*

$$\widetilde{\mathbf{F}}_{\mathrm{CR}} = \eta\widetilde{\mathbf{F}}_\mathrm{C} + (1-\eta)\widetilde{\mathbf{F}}_\mathrm{R}, \tag{23}$$

if $\mathbf{P} = \mathbf{I}_K$ and $K = N_\mathrm{S}$.

Algorithm 1 Hybrid beamforming for joint UM-MIMO radar-communications

Input: η, $\mathbf{F}_\mathrm{C}$, $\mathbf{F}_\mathrm{R}$.
Output: $\mathbf{F}_{\mathrm{RF}}$, $\mathbf{F}_{\mathrm{BB}}$.
1: Initialize with random $\mathbf{F}_{\mathrm{RF}} \in \mathbb{C}^{N_\mathrm{T} \times N_{\mathrm{RF}}}$, $\mathbf{F}_{\mathrm{BB}} \in \mathbb{C}^{N_{\mathrm{RF}} \times N_\mathrm{S}}$ and $\mathbf{P} \in \mathbb{C}^{K \times N_\mathrm{S}}$.
2: $\mathbf{F}_{\mathrm{CR}} = \eta\mathbf{F}_\mathrm{C} + (1-\eta)\mathbf{F}_\mathrm{R}\mathbf{P}$.
3: Construct $\mathcal{S}$ and $\bar{\mathcal{S}}$ depending on the structure of $\mathbf{F}_{\mathrm{RF}}$.
4: **while**
5: $\mathbf{P} = \widetilde{\mathbf{U}}\mathbf{I}_{K \times N_\mathrm{S}}\widetilde{\mathbf{V}}$, where $\widetilde{\mathbf{U}}\widetilde{\mathbf{\Sigma}}\widetilde{\mathbf{V}}^\mathsf{H} = \mathbf{F}_\mathrm{R}^\mathsf{H}\mathbf{F}_{\mathrm{RF}}\mathbf{F}_{\mathrm{BB}}$.
6: Compute $\mathbf{F}_{\mathrm{BB}}$ as $\mathbf{F}_{\mathrm{BB}} = \mathbf{F}_{\mathrm{RF}}^\dagger\mathbf{F}_{\mathrm{CR}}$ and normalize as $\mathbf{F}_{\mathrm{BB}} = \frac{\sqrt{N_\mathrm{S}}}{\|\mathbf{F}_{\mathrm{RF}}\mathbf{F}_{\mathrm{BB}}\|_\mathcal{F}}\mathbf{F}_{\mathrm{BB}}$.
7: Use $\mathcal{S}$ and $\bar{\mathcal{S}}$ and find $\mathbf{F}_{\mathrm{RF}}$ with the MMO algorithm in (16) and (18).
8: **until** convergence

Proof: If $\mathbf{P} = \mathbf{I}_\mathrm{K}$, then the solution of (16) involves the alternations between $\mathbf{F}_{\mathrm{RF}}$ and $\mathbf{F}_{\mathrm{BB}}$. Then, rewrite the cost function of (16) as

$$f(\widetilde{\mathbf{F}}_\mathrm{C}, \widetilde{\mathbf{F}}_\mathrm{R}) = \eta\|\widetilde{\mathbf{F}}_\mathrm{C} - \mathbf{F}_\mathrm{C}\|_\mathcal{F} + (1-\eta)\|\widetilde{\mathbf{F}}_\mathrm{R} - \mathbf{F}_\mathrm{R}\|_\mathcal{F}, \tag{24}$$

from which it is clear that $\widetilde{\mathbf{F}}_\mathrm{C}$ and $\widetilde{\mathbf{F}}_\mathrm{R}$ correspond to the communications- and radar-only solutions in (7) and (10) for $\eta = 1$ and $\eta = 0$, respectively. Using the inequality in (13), we use the following cost, which does not affect the solution, i.e.,

$$\begin{aligned}\bar{f}(\widetilde{\mathbf{F}}_\mathrm{C}, \widetilde{\mathbf{F}}_\mathrm{R}) &= \|\eta[\widetilde{\mathbf{F}}_\mathrm{C} - \mathbf{F}_\mathrm{C}] + (1-\eta)[\widetilde{\mathbf{F}}_\mathrm{R} - \mathbf{F}_\mathrm{R}]\|_\mathcal{F} \\ &= \|\eta\widetilde{\mathbf{F}}_\mathrm{C} + (1-\eta)\widetilde{\mathbf{F}}_\mathrm{R} - \eta\mathbf{F}_\mathrm{C} - (1-\eta)\mathbf{F}_\mathrm{R}\|_\mathcal{F} \\ &= \|\widetilde{\mathbf{F}}_{\mathrm{CR}} - \eta\mathbf{F}_\mathrm{C} - (1-\eta)\mathbf{F}_\mathrm{R}\|_\mathcal{F} \\ &= \|\widetilde{\mathbf{F}}_{\mathrm{CR}} - \mathbf{F}_{\mathrm{CR}}\|_\mathcal{F}, \end{aligned} \tag{25}$$

which gives (23) as the linear combination of $\widetilde{\mathbf{F}}_\mathrm{C}$ and $\widetilde{\mathbf{F}}_\mathrm{R}$ by depending on η. ■

This analysis allows us to design the JRC hybrid beamformer as a function of η after solving the communications- and radar-only problems (7) and (10), respectively, instead of solving (16) for every η.

B. Hybrid Beamformer Design With CCM

Instead of designing the hybrid beamformer $\mathbf{F}_{\mathrm{RF}}\mathbf{F}_{\mathrm{BB}}$ with respect to $\mathbf{H}$, the usage of the CCM provides lower channel overhead via infrequent updates of the THz channel information between the RX and the TX. However, this approach has the cost of slight performance loss in the spectral efficiency due to long-term statistics of the channel information. The usage of CCM is particularly helpful in THz transmission compared to the mm-Wave case due to smaller number of Los/non-LoS signal components, which reduces the angular spread of the received signals [22]. To exploit the structure of CCM-based hybrid beamforming, we first introduce the CCM model to derive the near-optimal unconstrained CCM-based beamformer $\bar{\mathbf{F}}_\mathrm{C} \in \mathbb{C}^{N_\mathrm{T} \times N_\mathrm{S}}$ via the eigendecomposition of the CCM $\mathbf{C} \in \mathbb{C}^{N_\mathrm{T} \times N_\mathrm{T}}$. Rewrite (2) as

$$\mathbf{H} = \gamma\mathbf{B}_\mathrm{R}\mathbf{\Gamma}\mathbf{B}_\mathrm{T}^\mathsf{H}, \tag{26}$$

where $\mathbf{B}_{\mathrm{R}} = [\mathbf{A}_{\mathrm{R}}(\Theta_1), \ldots, \mathbf{A}_{\mathrm{R}}(\Theta_L)] \in \mathbb{C}^{N_{\mathrm{R}} \times QL}$ and $\mathbf{B}_{\mathrm{T}} = [\mathbf{A}_{\mathrm{T}}(\Psi_1), \ldots, \mathbf{A}_{\mathrm{T}}(\Psi_L)] \in \mathbb{C}^{N_{\mathrm{T}} \times QL}$ steering matrices of L paths, respectively. $\mathbf{\Gamma} = \mathrm{blkdiag}\{\alpha_1 \mathbf{I}_Q, \ldots, \alpha_L \mathbf{I}_Q\} \in \mathbb{C}^{QL \times QL}$ is a diagonal matrix which includes the path gains. Using the property that the channel gains are independent random variables, we write the covariance of the channel at the TX, i.e., $\mathbf{C} = \mathbb{E}\{\mathbf{H}^{\mathsf{H}}\mathbf{H}\}$ as

$$\mathbf{C} = \gamma^2 \mathbb{E}_{\mathbf{H}}\{\mathbf{B}_{\mathrm{T}} \mathbf{\Gamma}^{\mathsf{H}} \mathbf{B}_{\mathrm{R}}^{\mathsf{H}} \mathbf{B}_{\mathrm{R}} \mathbf{\Gamma} \mathbf{B}_{\mathrm{T}}^{\mathsf{H}}\}, \tag{27}$$

where the expectation is performed over $\mathbf{H}$. Taking statistical expectation over the AoA/AoD angles and the channel gains, respectively, (27) becomes

$$\mathbf{C} = \gamma^2 \mathbb{E}_{\Psi}\{\mathbf{B}_{\mathrm{T}} \mathbb{E}_{\alpha}\{\mathbf{\Gamma}^{\mathsf{H}} \mathbb{E}_{\Theta}\{\mathbf{B}_{\mathrm{R}}^{\mathsf{H}} \mathbf{B}_{\mathrm{R}}\} \mathbf{\Gamma}\} \mathbf{B}_{\mathrm{T}}^{\mathsf{H}}\}, \tag{28}$$

for which we have $\mathbb{E}_{\Theta}\{\mathbf{B}_{\mathrm{R}}^{\mathsf{H}} \mathbf{B}_{\mathrm{R}}\} = \mathbf{I}_{QL}$ and $\mathbb{E}_{\alpha}\{\mathbf{\Gamma}^{\mathsf{H}} \mathbf{\Gamma}\} = \widetilde{\mathbf{\Gamma}} = \mathrm{blkdiag}\{\sigma_{\alpha_1}^2 \mathbf{I}_{\mathrm{Q}}, \ldots, \sigma_{\alpha_L}^2 \mathbf{I}_{\mathrm{Q}}\}$ due to the independent zero-mean channel gains. Thus, we finally get

$$\mathbf{C} = \gamma^2 \mathbf{B}_{\mathrm{T}} \widetilde{\mathbf{\Gamma}} \mathbf{B}_{\mathrm{T}}^{\mathsf{H}} = \gamma^2 \sum_{l=1}^{L} \sigma_{\alpha_l}^2 \mathbb{E}\{\mathbf{A}_{\mathrm{T}}(\Psi_l) \mathbf{A}_{\mathrm{T}}^{\mathsf{H}}(\Psi_l)\}. \tag{29}$$

Compared to the CSI in (2), the CCM in (29) only preserves the channel statistics, such as variance of received path gains at the TX. While the CCM does not provide us the complete instantaneous channel knowledge as of $\mathbf{H}$, it has lower channel feedback since the RX only needs to send $\{\sigma_{\alpha_l}^2\}_{l=1}^{L}$, mean AoD angles $\{\bar{\Psi}_l\}_{l=1}^{L}$ and angular spreads $\{\sigma_{\Psi_l}\}_{l=1}^{L}$ infrequently, instead of sending the precise knowledge of $\mathbf{H}$. Then, the covariance matrix at the TX is constructed as

$$\mathbf{C} = \gamma^2 \sum_{l=1}^{L} \int_{\bar{\Psi}_l - \frac{\sigma_{\Psi_l}}{2}}^{\bar{\Psi}_l + \frac{\sigma_{\Psi_l}}{2}} \sigma_{\alpha_l}^2 \mathbf{A}_{\mathrm{T}}(\Psi) \mathbf{A}_{\mathrm{T}}^{\mathsf{H}}(\Psi) d\Psi. \tag{30}$$

Then, the optimal unconstrained statistical beamformer $\bar{\mathbf{F}}_{\mathrm{C}} \in \mathbb{C}^{N_{\mathrm{T}} \times N_{\mathrm{S}}}$ is designed via the following quadratic problem, i.e.,

$$\bar{\mathbf{F}}_{\mathrm{C}} = \arg\max_{\tilde{\mathbf{F}}} \; ||\tilde{\mathbf{F}}^{\mathsf{H}} \mathbf{C} \tilde{\mathbf{F}}||_{\mathcal{F}}, \quad \text{s. t.:} \; ||\tilde{\mathbf{F}}||_{\mathcal{F}} = N_{\mathrm{S}}, \tag{31}$$

whose solution is readily found as the linear combination of the eigenvectors corresponding to the N_{S} strongest paths [58].

Once the unconstrained statistical beamformer is obtained, the next task is to determine the analog precoder $\mathbf{F}_{\mathrm{RF}}$. One possible solution is to solve

$$\min_{\mathbf{F}_{\mathrm{RF}}} \; ||\mathbf{F}_{\mathrm{RF}} - \bar{\mathbf{F}}_{\mathrm{CR}}||_{\mathcal{F}}, \quad \text{s. t.:} \; |[\mathbf{F}_{\mathrm{RF}}]_{i,j}| = \frac{1}{\sqrt{N_{\mathrm{T}}}}, \tag{32}$$

where $\bar{\mathbf{F}}_{\mathrm{CR}} = \eta \bar{\mathbf{F}}_{\mathrm{C}} + (1-\eta) \mathbf{F}_{\mathrm{R}} \mathbf{P}$, and then estimate $\mathbf{F}_{\mathrm{BB}}$ and $\mathbf{P}$. The solution to (32) is readily obtained as $\mathbf{F}_{\mathrm{RF}} = \frac{1}{\sqrt{N_{\mathrm{T}}}} \exp\{j \angle \bar{\mathbf{F}}_{\mathrm{CR}}\}$, which takes only the phase information of $\bar{\mathbf{F}}_{\mathrm{CR}}$ [1, 50]. However, this approach is sub-optimum. Furthermore, its performance becomes significantly poor as N_{S} increases [50, 58]. The optimum solution is obtained by solving

$$\begin{aligned} \min_{\mathbf{F}_{\mathrm{RF}}, \mathbf{F}_{\mathrm{BB}}} \; & \big|\big|\mathbf{F}_{\mathrm{RF}} \mathbf{F}_{\mathrm{BB}} - \bar{\mathbf{F}}_{\mathrm{CR}}\big|\big|_{\mathcal{F}} \\ \text{s. t.:} \; & |[\mathbf{F}_{\mathrm{RF}}]_{i,j}| = \frac{1}{\sqrt{N_{\mathrm{T}}}}, \\ & \big|\big|\mathbf{F}_{\mathrm{RF}} \mathbf{F}_{\mathrm{BB}}\big|\big|_{\mathcal{F}} = N_{\mathrm{S}}. \end{aligned} \tag{33}$$

which is similar to (16) and the solution is obtained by following the similar procedure presented in Algorithm 1 by replacing $\mathbf{F}_{\mathrm{C}}$ with $\bar{\mathbf{F}}_{\mathrm{C}}$.

C. Extension to Broadband Hybrid Beamforming

Due to the large bandwidth available in THz band, the implementation of broadband hybrid beamformers in multi-carrier UM-MIMO-OFDM scenario is very critical. In this case, the hybrid beamformers are comprised of a single RF precoder $\mathbf{F}_{\mathrm{RF}}$ while there are subcarrier-dependent baseband beamformers, e.g., $\mathbf{F}_{\mathrm{BB}}[m]$, $m \in \{1, \ldots, M\}$, where M is the number of OFDM subcarriers. The rationale behind using a single RF precoder is that the operating frequency is relatively higher than the bandwidth in THz systems and the subcarrier frequencies are close to each other, (i.e., $f_{m_1} \approx f_{m_2}$, $m_1, m_2 \in \{1, \ldots, M\}$), thus the generated beams are almost identical. Hence, we use a single operating wavelength $\lambda = \lambda_1 = \cdots = \lambda_M = \frac{c_0}{f_c}$ where c_0 is speed of light and f_c is the central carrier frequency [41]. As a result, the transmitted signal becomes $\mathbf{x}[m] = \mathbf{F}_{\mathrm{RF}} \mathbf{F}_{\mathrm{BB}}[m] \mathbf{s}[m]$, which is received at the RX as

$$\mathbf{y}[m] = \sqrt{\rho} \mathbf{H}[m] \mathbf{F}_{\mathrm{RF}} \mathbf{F}_{\mathrm{BB}}[m] \mathbf{s}[m] + \mathbf{n}[m]. \tag{34}$$

In broadband scenario, the channel matrix $\mathbf{H}[m]$ includes the contributions of L paths, each of which has the time delay τ_l, and denote $p(\tau)$ as a pulse shaping function for T_{s}-spaced signaling evaluated at τ seconds, then the THz delay-d UM-MIMO channel matrix is

$$\mathbf{H}[d] = \gamma \sum_{l=1}^{L} \alpha_l p(dT_{\mathrm{s}} - \tau_l) \mathbf{A}_{\mathrm{R}}(\Theta_l) \mathbf{A}_{\mathrm{T}}^{\mathsf{H}}(\Psi_l), \tag{35}$$

which is then processed by M-point DFT, and the channel matrix at subcarrier m becomes $\mathbf{H}[m] = \sum_{d=0}^{D-1} \mathbf{H}[d] e^{-j \frac{2\pi m}{M} d}$, where D is the length of cyclic prefix. The frequency domain channel is then used in UM-MIMO-OFDM systems, where the orthogonality of each subcarrier is enforced such that $||\mathbf{H}^{\mathsf{H}}[m_1] \mathbf{H}[m_2]||_{\mathcal{F}} = 0$ for $m_1 \neq m_2$.

In CSI-based scenario, the hybrid precoders $\mathbf{F}_{\mathrm{RF}}$ and $\mathbf{F}_{\mathrm{BB}}[m]$ is designed by modifying the problem (16) as

$$\begin{aligned} \min_{\mathbf{F}_{\mathrm{RF}}, \widetilde{\mathbf{F}}_{\mathrm{BB}}, \widetilde{\mathbf{P}}} \; & \|\mathbf{F}_{\mathrm{RF}} \widetilde{\mathbf{F}}_{\mathrm{BB}} - \widetilde{\mathbf{F}}_{\mathrm{CR}}\|_{\mathcal{F}} \\ \text{s. t.:} \; & \|\mathbf{F}_{\mathrm{RF}} \widetilde{\mathbf{F}}_{\mathrm{BB}}\|_{\mathcal{F}} = M N_{\mathrm{S}}, \\ & |[\mathbf{F}_{\mathrm{RF}}]_{i,j}| = \frac{1}{\sqrt{N_{\mathrm{T}}}}, \;\; \forall i,j \in \mathcal{S}, \\ & |[\mathbf{F}_{\mathrm{RF}}]_{i,j}| = 0, \;\; \forall i,j \in \bar{\mathcal{S}}, \\ & \widetilde{\mathbf{P}} \widetilde{\mathbf{P}}^{\mathsf{H}} = \mathbf{I}_{M N_{\mathrm{S}}}, \end{aligned} \tag{36}$$

where $\widetilde{\mathbf{P}}$ is a $K \times M N_{\mathrm{S}}$ matrix and we have $\widetilde{\mathbf{F}}_{\mathrm{CR}} = \big[\mathbf{F}_{\mathrm{CR}}[1] \;\; \mathbf{F}_{\mathrm{CR}}[2] \;\; \cdots \;\; \mathbf{F}_{\mathrm{CR}}[M]\big]$ and $\widetilde{\mathbf{F}}_{\mathrm{BB}} = \big[\mathbf{F}_{\mathrm{BB}}[1] \;\; \mathbf{F}_{\mathrm{BB}}[2] \;\; \cdots \;\; \mathbf{F}_{\mathrm{BB}}[M]\big]$ containing the beamformers for all subcarriers. $\mathbf{F}_{\mathrm{CR}}[m]$ corresponds to the unconstrained radar-communications beamformer as $\mathbf{F}_{\mathrm{CR}}[m] = \eta \mathbf{F}_{\mathrm{C}}[m] + (1-\eta) \mathbf{F}_{\mathrm{R}} \mathbf{P}$, in which only $\mathbf{F}_{\mathrm{C}}[m]$ depends on m and it is obtained from the right singular matrix of $\mathbf{H}[m]$.

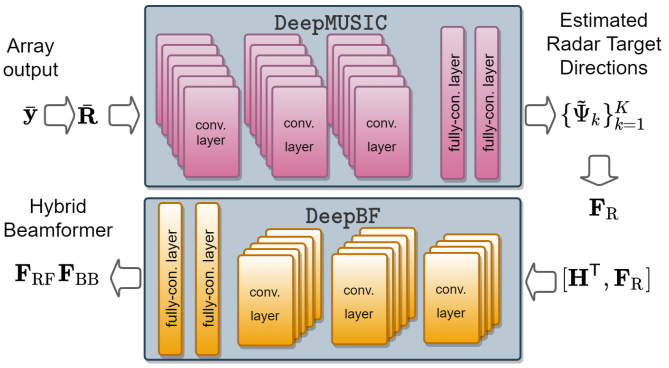

Fig. 3. Model-free hybrid beamforming framework, in which DeepMUSIC [49] and DeepBF are employed to predict radar target directions and hybrid beamformer weights, respectively.

The CCM-based counterpart of the problem (36) is designed similar to (33) and they are solved effectively via MMO depending on the array structure, e.g., FC, PC or PCO.

IV. Model-Free Hybrid Beamforming

In this section, we introduce our model-free approach for hybrid beamforming by designing a CNN model. While the design of the learning model is relatively easier for communications-only [45, 53] and radar-only [49] problems, the joint scenario involves several matrix variables, such as $\mathbf{H}$, $\mathbf{F}_{\mathrm{C}}$, $\mathbf{F}_{\mathrm{RF}}$, $\mathbf{F}_{\mathrm{BB}}$, $\mathbf{F}_{\mathrm{R}}$ and $\mathbf{P}$, which make the problem very challenging. Another difficulty is due to the size of these variables, which are huge because of the large number of antennas deployed in THz scenario.

To efficiently train the model while maintaining satisfactory learning performance, we first adopt the DeepMUSIC model of [49] to estimate the radar target directions and construct $\mathbf{F}_{\mathrm{R}}$, as shown in Fig. 3. To this end, the array output at the TX is utilized. The radar collects the reflected signal from the targets as

$$\bar{\mathbf{y}}(t_i) = \sum_{k=1}^{K} \mathbf{W}_{\mathrm{RF}}\mathbf{a}_{\mathrm{T}}(\Phi_k)\mathbf{a}_{\mathrm{T}}^{\mathsf{T}}(\Phi_k)r_k(t_i) + \mathbf{W}_{\mathrm{RF}}\bar{\mathbf{n}}(t_i), \quad (37)$$

where t_i denotes the sample index for $i = 1, \ldots, T_R$, where T_R is the number of snapshots, $r_k(t_i)$ represents the reflection coefficient of the transmitted signal corresponding to the kth target, and $\bar{\mathbf{n}}(t_i)$ denotes the $N_{\mathrm{T}} \times 1$ noise term. $\mathbf{W}_{\mathrm{RF}}\mathbf{a}_{\mathrm{T}}(\Phi_k)$ denotes the actual steering vector after processing via the analog combiner $\mathbf{W}_{\mathrm{RF}} \in \mathbb{C}^{N_{\mathrm{RF}} \times N_{\mathrm{T}}}$ [44]. Then, the sample covariance matrix is computed as $\bar{\mathbf{R}} = \frac{1}{T_R}\sum_{i=1}^{T_R} \bar{\mathbf{y}}(t_i)\bar{\mathbf{y}}^{\mathsf{H}}(t_i)$. $\bar{\mathbf{R}}$ is input to DeepMUSIC to obtain the MUSIC spectra at the output [49]. After performing peak-finding on the resultant spectra, the estimated target locations are acquired and the corresponding $\mathbf{F}_{\mathrm{RF}}$ are constructed.

To obtain the hybrid beamformers, we design another model, which is called DeepBF (Fig. 3), for which $\mathbf{F}_{\mathrm{R}}$ is utilized together with the channel matrix $\mathbf{H}$ to represent the inputs for radar- and communications-only tasks, respectively. The input of DeepBF is then $\boldsymbol{\Xi} = [\mathbf{H}^{\mathsf{T}}, \mathbf{F}_{\mathrm{R}}] \in \mathbb{C}^{N_{\mathrm{T}} \times (N_{\mathrm{R}}+K)}$.

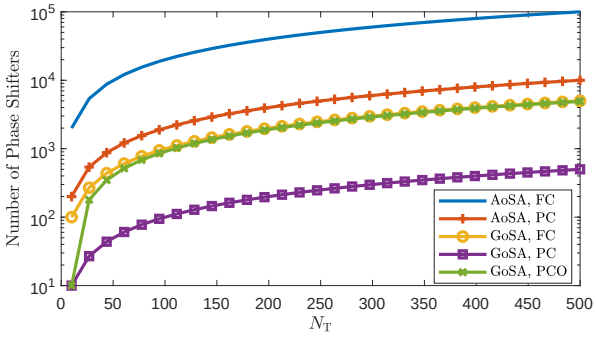

(a)

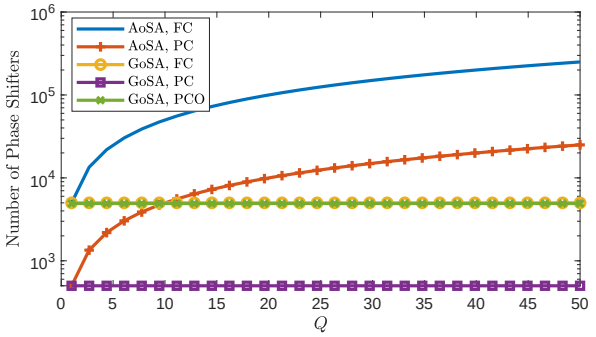

(b)

Fig. 4. Number of phase-shifters versus (a) N_{T} when $Q = 20$ and (b) Q when $N_{\mathrm{T}} = 500$ for $N_{\mathrm{RF}} = 10$.

If PC array is assumed, then $\mathbf{F}_{\mathrm{R}}$ is squeezed into a vector yielding an $N_{\mathrm{T}} \times (N_{\mathrm{R}} + 1)$ input. The "channels" of DeepBF are designed as the real, imaginary values of $\boldsymbol{\Xi}$, the input size of DeepBF is $N_{\mathrm{T}} \times (N_{\mathrm{R}} + K) \times 2$ for a single data sample. The output of DeepBF is designed as the real and imaginary values of the hybrid beamformer $\mathbf{F}_{\mathrm{RF}}\mathbf{F}_{\mathrm{BB}}$, i.e., $\boldsymbol{\xi} = [\mathrm{vec}\{\mathrm{Re}\{\mathbf{F}_{\mathrm{RF}}\mathbf{F}_{\mathrm{BB}}\}\}^{\mathsf{T}}, \mathrm{vec}\{\mathrm{Im}\{\mathbf{F}_{\mathrm{RF}}\mathbf{F}_{\mathrm{BB}}\}\}^{\mathsf{T}}]^{\mathsf{T}} \in \mathbb{R}^{2N_{\mathrm{T}}N_{\mathrm{S}}}$. Thus, the learning model constructs the non-linear relationship $\mathcal{L} : \mathbb{R}^{N_{\mathrm{T}} \times (N_{\mathrm{R}}+K)} \rightarrow \mathbb{R}^{2N_{\mathrm{T}}N_{\mathrm{S}}}$ as $\mathcal{L}(\boldsymbol{\Xi}, \boldsymbol{\theta}) = \boldsymbol{\xi}$, where $\boldsymbol{\theta}$ represents the learnable parameters of DeepBF.

V. Numerical Experiments

In this section, we evaluate the performance of the proposed hybrid beamforming approach for different array structures. The communications performance of the algorithms is evaluated in terms of spectral efficiency while the radar performance is presented with the beampattern analysis of the hybrid beamformers. Furthermore, we analyze the trade-off between both tasks by sweeping η for $[0, 1]$. The hybrid beamformers are designed for FC, PC and PCO array structures. The proposed MMO-based approach is used to design PCO array. Then, it is compared with the PC and FC arrays, which employ the MO-based alternating minimization (MO-AltMin) [37] and triple AltMin (TAltMin) approach in [51], respectively, while the fully digital unconstrained beamformers are used as a benchmark [1].

In the simulations, unless stated otherwise, we select the operating frequency as $f_c = 300$ GHz, which is in low-THz band (100 GHz - 1 THz) and applicable for long range radar

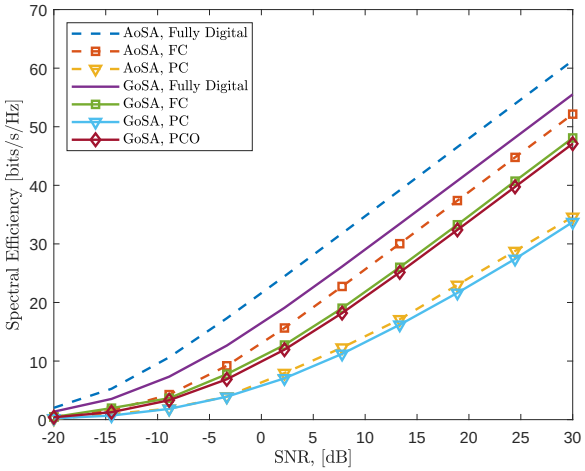

Fig. 5. Spectral efficiency versus SNR for CSI-based beamforming when $\eta = 0.5$.

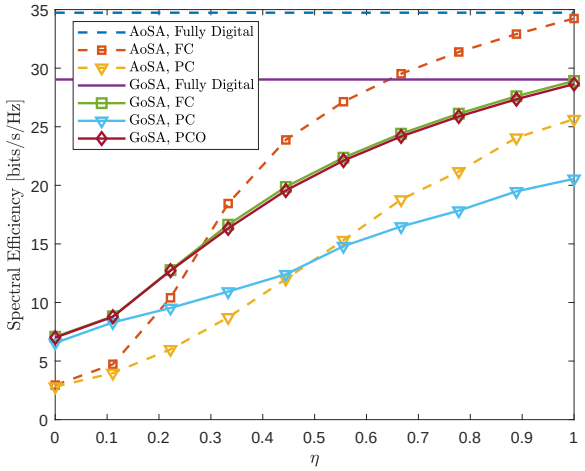

Fig. 6. Spectral efficiency versus η for SNR= 10 dB.

(LRR) ($\sim$ 150 m) [59]. We also select $\Delta = \Delta_{\rm x} = \Delta_{\rm y} = \lambda/2$ and $\delta = \delta_{\rm x} = \delta_{\rm y} = \lambda/4$. At the TX and RX, $N_{\rm T_x} = N_{\rm T_y} = 32$ ($N_{\rm T} = 1024$) and $N_{\rm R_x} = N_{\rm R_y} = 9$ ($N_{\rm R} = 81$) subarrays are used, respectively, with $Q_{\rm x} = Q_{\rm y} = 3$ ($Q = 9$). Thus, the resultant architecture forms a 729×9216 UM-MIMO transceiver. We assume that $N_{\rm RF} = 16$ RF chains are used at the TX to transmit $N_{\rm S} = 4$ data streams to the RX via the THz channel which is assumed to include $L = 5$ paths, where $\phi_l, \varphi_l \in [-150°, 150°]$ and $\theta_l, \vartheta_l \in [70°, 90°]$. The TX simultaneously generates beams towards both RX and $K = 3$ radar targets located at $\{(60°, 70°), (110°, 75°), (140°, 80°)\}$.

The learning model `DeepBF` is realized as a CNN with 11 layers. The first layer is the input layer of size $N_{\rm T} \times (N_{\rm R} + K) \times 2$. The second, fourth and sixth layers are convolutional layers with $256@3 \times 3$ filters. After first two convolutional layers, there is a max-pooling to reduce dimension by 2. The seventh and ninth layers are fully connected layers with 1024 units. The eighth and tenth layers are dropout layers with 50% rate. Finally, the last layer is a regression layer of size $2N_{\rm T}N_{\rm S}$. The training data is generated for $Z_{\rm C} = 10^2$ channel realizations with the aforementioned channel statistics and $K = 3$ radar target directions, which are generated uniform randomly from the interval $[-50°, 50°]$ with $1°$ resolution for $Z_{\rm R} = 10^4$ realizations. For model-free approach, we consider 1-D scenario, i.e., the elevation angles of the targets are $90°$ for simplicity. As a result, the resulting dataset is comprised of $Z_{\rm C}Z_{\rm R} = 10^6$ samples of size $N_{\rm T} \times (N_{\rm R} + K) \times 2$. The `DeepMUSIC` model is trained as described in [49].

Fig. 4 shows the number of phase-shifters with respect to $N_{\rm T}$ and Q for different array structures, i.e., AoSA and GoSA, respectively. The FC structures employ $N_{\rm T}QN_{\rm RF}$ and $N_{\rm T}N_{\rm RF}$ phase-shifters for AoSA and GoSA, respectively, while the PC structures are more efficient since only $N_{\rm T}Q$ and $N_{\rm T}$ phase-shifters are used for AoSA and GoSA. Compared to AoSA, the proposed GoSA structure employs much less phase-shifters than that of AoSA for $Q \geq N_{\rm RF}$ and they become equal if $Q = 1$. Thus, GoSA is much more energy-efficient

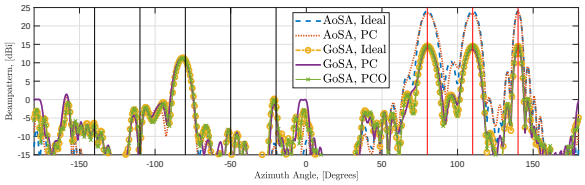

(a)

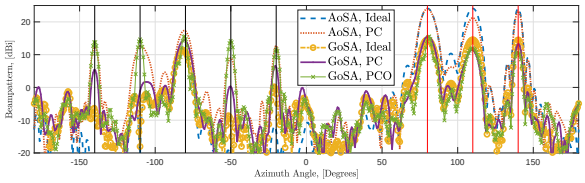

(b)

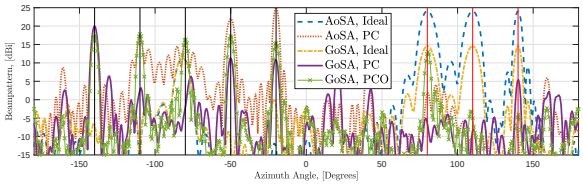

(c)

Fig. 7. Beampattern in the azimuth plane for (a) $\eta = 0$, (b) $\eta = 0.5$ and (c) $\eta = 1$, when the radar targets are located at $\{(80°, 90°), (110°, 90°), (140°, 90°)\}$ and the communications paths are received from $\{(-20°, 90°), (-50°, 90°), (-80°, 90°), (-110°, 90°), (-140°, 90°)\}$, which are depicted by red and black vertical lines, respectively.

than AoSA. While GoSA provides lower hardware complexity, it has slightly poorer spectral efficiency performance, which is ameliorated via the PCO structure by increasing the number of phase-shifters from $N_{\rm T}$ (non-overlapped) up to $N_{\rm RF}(N_{\rm T} - N_{\rm RF} + 1)$ (fully-overlapped). Nevertheless, the fully-overlapped or fully-connected GoSAs still have lower phase-shifters than that of AoSA with PC.

Fig. 5 shows the spectral efficiency with respect to SNR for CSI-based hybrid beamforming when $\eta = 0.5$. We observe

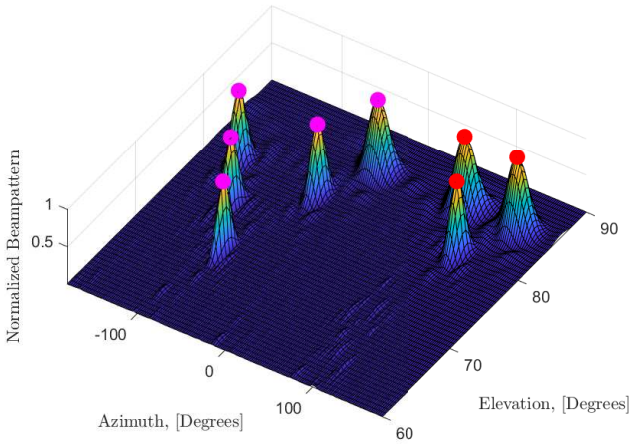

Fig. 8. Beampattern in 2-D plane for $\eta = 0.5$. The radar target are located at $\{(80°, 85°), (110°, 80°), (140°, 85°)\}$ and the communications paths are received from $\{(-20°, 85°), (-50°, 80°), (-80°, 70°), (-110°, 75°), (-140°, 80°)\}$, which are illustrated with red and pink colors, respectively.

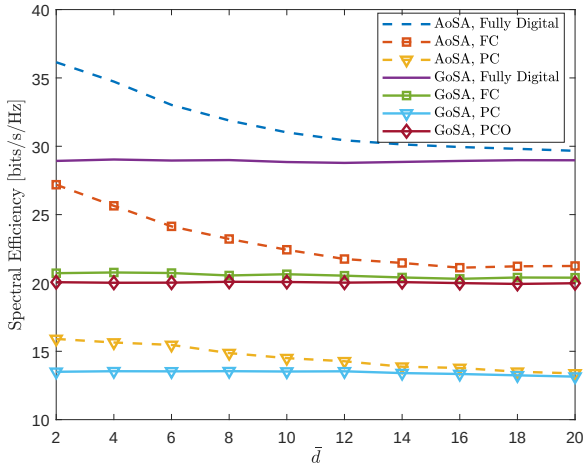

Fig. 9. Spectral efficiency versus $\bar{d}$ for SNR= 10 dB when $\eta = 0.5$.

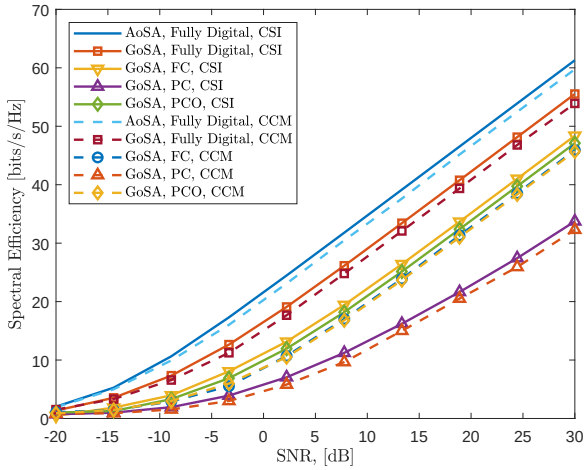

Fig. 10. Spectral efficiency versus SNR for CCM-based beamforming when $\eta = 0.5$.

that GoSA performs slightly lower than AoSA structure while using $Q = 9$ times less phase-shifters, which significantly lowers the hardware complexity of UM-MIMO system. While PC structures have the lowest hardware complexities, they perform the worst as compared to FC case. The GoSA with PCO improves the spectral efficiency by employing relatively more phase-shifters which still less than that of AoSA. The gap between the unconstrained (fully digital) and hybrid beamformers is large due to the trade-off between radar and communications tasks with $\eta = 0.5$.

In Fig. 6, the spectral efficiency is presented with respect to η, wherein we note that as $\eta \to 1$, the spectral efficiency for the FC, PC and PCO approaches to the performance of unconstrained beamformer, i.e., $\mathbf{F}_{\mathrm{C}}$. When $\eta \to 0$, then the RF precoder $\mathbf{F}_{\mathrm{RF}}$ generates the beams towards the radar targets only, thus the spectral efficiency is reduced. As a result, the selection of η is critical. In practice, η is increased if the communications task is more critical than tracking the targets or when there is no target. Conversely, lower η is selected if the radar task demands more resources, e.g., more transmit power is required depending on the range of the radar targets.

We illustrate the beampattern of the designed hybrid beamformers in Fig. 7 and Fig. 8 for 1-D and 2-D angle distributions, respectively. In Fig. 7, the beampatterns are presented for $\eta = 0$, $\eta = 0.5$ and $\eta = 1$, where we assume that the all of the paths have the elevation angle of 90°. The ideal beampatterns correspond to the radar-only beamformer $\mathbf{F}_{\mathrm{R}}$ for AoSA and GoSA structures. We note that for $\eta = 0$ ($\eta = 1$) all the beams are generated towards the radar targets (the RX), respectively, while $\mathbf{F}_{\mathrm{RF}}$ generates $L + K$ beams towards both targets and the RX when $\eta = 0.5$. The proposed GoSA PCO structure provides narrower beams towards bot RX and radar targets as compared to the other algorithms. The 2-D angular distribution is illustrated in Fig. 8 for $\eta = 0.5$, where we present the beampattern corresponding to the GoSA with PCO. We observe that the proposed hybrid beamforming approach accurately generates beams towards both targets and RX paths in 2-D angular space. This is provided with the 2-D structure of the antenna array in two dimensions.

While the design of the antenna array is straightforward in AoSA case by selecting the antenna spacing as $\lambda/2$, the selection of δ is critical for the GoSA structure illustrated in Fig. 1. In Fig. 9, we present the spectral efficiency performance with respect to $\bar{d}$, where $\bar{d} = \frac{\lambda}{\delta}$. As $\bar{d}$ increases, we reduce the antenna element spacing in the subarrays of GoSA. Specifically, when $\bar{d} = \infty$, we have $\delta = 0$, thus the $Q_{\mathrm{x}} \times Q_{\mathrm{y}}$ antennas in each subarray become co-located. We infer this from Fig. 9 as the performance of AoSA approaches to that of GoSA as $\bar{d}$ increases. While slight performance loss is observed from AoSA with PC, the performance of the FC structure and the fully digital beamformers significantly reduce as $\bar{d}$

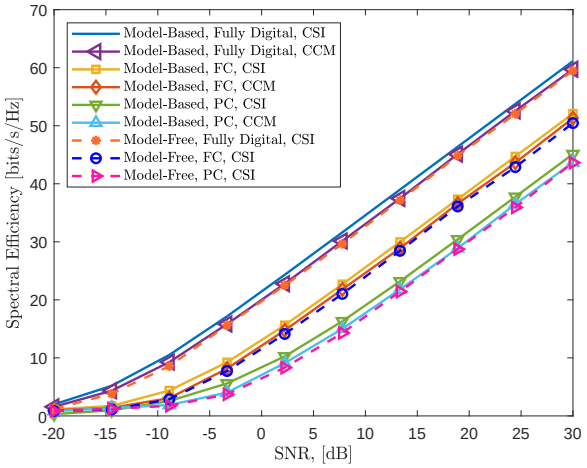

Fig. 11. Spectral efficiency for model-based and model-free hybrid beamformer design when $\eta = 0.5$.

increases. As a result, this figure is helpful when designing the GoSA because of the improvement in the spectral efficiency by changing $\bar{d}$ while the lower limit is $\bar{d} = 2$ (i.e., $\delta = \lambda/2$) to avoid spatial aliasing among the antennas.

In order to construct the CCM, we select $\sigma_{\Psi_l} = 5^\circ$, $\forall l$, angular spreads for both azimuth and elevation angles as in (30). Fig. 10 shows the spectral efficiency of the competing algorithms for both CSI- and CCM-based beamforming when $\eta = 0.5$. A slight performance loss is observed for all CCM-based approaches due to loss of precision in the angle and path gain information while less channel overhead is involved in CCM-based beamforming. In particular, in the CSI-based approach, the RX should feedback $N_{\mathrm{R}}Q \times N_{\mathrm{T}}Q$ (729×9216) channel matrix whereas only the angle and path information of size L needs to be sent to the TX in the CCM so that $\mathbf{C}$ is constructed as in (30).

Fig. 11 shows the spectral efficiency comparison of model-based and model-free techniques when GoSA structure is used. The simulations are averaged over, 500 Monte Carlo trials, each of which is conducted for different realization of radar target angles. While a slight loss is observed for the model-free techniques compared to CSI-based beamforming, they have close performance to the CCM-based methods. Another advantage of the model-based approach is computational complexity thanks to its implementation via parallel processing units, such as GPUs. Based on simulations for the aforementioned TX-RX settings, the computation time for MO, TAltMin, `DeepMUSIC` and `DeepBF` are 2.124, 0.68, 0.0036 and 0.0058 seconds, which shows the advantage of model-free techniques. For further analysis on the complexity order of model-based (i.e., MO, TAltMin) and model-free techniques, we refer the reader to [37, 51] and [53].

VI. Summary

In this paper, we introduced THz UM-MIMO JRC architecture and investigate model-based and model-free hybrid beamforming techniques. To lower the hardware complexity critical in THz systems, we proposed GoSA UM-MIMO architecture. We developed hybrid beamforming via PCO structures to provide a trade-off between higher spectral efficiency and hardware complexity in terms of the number of phase-shifters. The hybrid beamformers for THz JRC system are designed relying on both CSI and CCM of the wireless channel information between the TX and the RX. The computation times for beamformer design could be prohibitively high for UM-MIMO THz systems. We addressed this by suggesting a model-free DL-based approach.

We evaluated the performance of the proposed methods in terms of spectral efficiency and radar beampattern. We demonstrated that GoSA provides less hardware complexity compared to full array and AoSA structures. Compared to CSI-based beamforming, CCM-based approach has a slight performance loss, while the latter enjoys less channel overhead. The model-free method is advantageous in terms of computational complexity and exhibits approximately 500 times lower computation time as compared to the MO-based approaches, while maintaining spectral efficiency performance close to that of CCM-based technique.

References

[1] R. W. Heath, N. Gonzalez-Prelcic, S. Rangan, W. Roh, and A. M. Sayeed, "An overview of signal processing techniques for millimeter wave MIMO systems," *IEEE J. Sel. Topics Signal Process.*, vol. 10, no. 3, pp. 436–453, 2016.

[2] K. V. Mishra, M. R. Bhavani Shankar, V. Koivunen, B. Ottersten, and S. A. Vorobyov, "Toward millimeter wave joint radar-communications: A signal processing perspective," *IEEE Signal Process. Mag.*, vol. 36, no. 5, pp. 100–114, 2019.

[3] N. Rajatheva, I. Atzeni, E. Bjornson, A. Bourdoux, S. Buzzi, J.-B. Dore, S. Erkucuk, M. Fuentes, K. Guan, Y. Hu *et al.*, "White paper on broadband connectivity in 6G," *arXiv preprint arXiv:2004.14247*, 2020.

[4] H.-J. Song and T. Nagatsuma, "Present and future of terahertz communications," *IEEE Trans. THz Sci. Technol.*, vol. 1, no. 1, pp. 256–263, 2011.

[5] I. F. Akyildiz and J. M. Jornet, "Realizing ultra-massive MIMO (1024× 1024) communication in the (0.06-10) terahertz band," *Nano Communication Networks*, vol. 8, pp. 46–54, 2016.

[6] T. Kürner and S. Priebe, "Towards THz communications-status in research, standardization and regulation," *Journal of Infrared, Millimeter, and Terahertz Waves*, vol. 35, no. 1, pp. 53–62, 2014.

[7] K. Tekbıyık, A. R. Ekti, G. K. Kurt, and A. Görçin, "Terahertz band communication systems: Challenges, novelties and standardization efforts," *Physical Communication*, vol. 35, p. 100700, 2019.

[8] S. H. Dokhanchi, B. S. Mysore, K. V. Mishra, and B. Ottersten, "A mmWave automotive joint radar-communications system," *IEEE Trans. Aerosp. Electron. Syst.*, vol. 55, no. 3, pp. 1241–1260, 2019.

[9] G. Wang and K. V. Mishra, "Displaced sensor automotive radar imaging," *arXiv preprint arXiv:2010.04085*, 2020.

[10] E. Marchetti, R. Du, B. Willetts, F. Norouzian, E. G. Hoare, T. Y. Tran, N. Clarke, M. Cherniakov, and M. Gashinova, "Radar cross-section of pedestrians in the low-THz band," *IET Radar, Sonar & Navigation*, vol. 12, no. 10, pp. 1104–1113, 2018.

[11] A. Faisal, H. Sarieddeen, H. Dahrouj, T. Y. Al-Naffouri, and M.-S. Alouini, "Ultramassive MIMO systems at Terahertz bands: Prospects and challenges," *IEEE Veh. Technol. Mag.*, vol. 15, no. 4, pp. 33–42, 2020.

[12] F. Norouzian, R. Du, E. G. Hoare, P. Gardner, C. Constantinou, M. Cherniakov, and M. Gashinova, "Low-THz transmission through water-containing contaminants on antenna radome," *IEEE Trans. THz Sci. Technol.*, vol. 8, no. 1, pp. 63–75, 2017.

[13] C. A. Schmuttenmaer, "Exploring dynamics in the far-infrared with terahertz spectroscopy," *Chemical Reviews*, vol. 104, no. 4, pp. 1759–1780, 2004.

[14] J. Sun, F. Hu, and S. Lucyszyn, "Predicting atmospheric attenuation under pristine conditions between 0.1 and 100 THz," *IEEE Access*, vol. 4, pp. 9377–9399, 2016.

[15] R. Piesiewicz, C. Jansen, D. Mittleman, T. Kleine-Ostmann, M. Koch, and T. Kurner, "Scattering analysis for the modeling of THz communication systems," *IEEE Trans. Antennas Propag.*, vol. 55, no. 11, pp. 3002–3009, 2007.

[16] Z. Xu and T. Liu, "Vital sign sensing method based on EMD in terahertz band," *EURASIP Journal on Advances in Signal Processing*, vol. 2014, no. 1, pp. 1–8, 2014.

[17] G. Ok, K. Park, H. J. Kim, H. S. Chun, and S.-W. Choi, "High-speed terahertz imaging toward food quality inspection," *Applied Optics*, vol. 53, no. 7, pp. 1406–1412, 2014.

[18] R. Appleby and H. B. Wallace, "Standoff detection of weapons and contraband in the 100 GHz to 1 THz region," *IEEE Trans. Antennas Propag.*, vol. 55, no. 11, pp. 2944–2956, 2007.

[19] F. Norouzian, E. Marchetti, M. Gashinova, E. Hoare, C. Constantinou, P. Gardner, and M. Cherniakov, "Rain attenuation at millimeter wave and low-THz frequencies," *IEEE Trans. Antennas Propag.*, vol. 68, no. 1, pp. 421–431, 2019.

[20] F. Norouzian, E. Marchetti, E. Hoare, M. Gashinova, C. Constantinou, P. Gardner, and M. Cherniakov, "Experimental study on low-THz automotive radar signal attenuation during snowfall," *IET Radar, Sonar & Navigation*, vol. 13, no. 9, pp. 1421–1427, 2019.

[21] R. Appleby and R. N. Anderton, "Millimeter-wave and submillimeter-wave imaging for security and surveillance," *Proc. IEEE*, vol. 95, no. 8, pp. 1683–1690, 2007.

[22] H. Sarieddeen, M.-S. Alouini, and T. Y. Al-Naffouri, "An overview of signal processing techniques for terahertz communications," *arXiv*, May 2020.

[23] L. Ju, B. Geng, J. Horng, C. Girit, M. Martin, Z. Hao, H. A. Bechtel, X. Liang, A. Zettl, Y. R. Shen *et al.*, "Graphene plasmonics for tunable terahertz metamaterials," *Nature nanotechnology*, vol. 6, no. 10, pp. 630–634, 2011.

[24] Z. Xu, X. Dong, and J. Bornemann, "Design of a reconfigurable MIMO system for THz communications based on graphene antennas," *IEEE Trans. THz Sci. Technol.*, vol. 4, no. 5, pp. 609–617, 2014.

[25] M. Moccia, C. Koral, G. P. Papari, S. Liu, L. Zhang, R. Y. Wu, G. Castaldi, T. J. Cui, V. Galdi, and A. Andreone, "Suboptimal coding metasurfaces for terahertz diffuse scattering," *Scientific reports*, vol. 8, no. 1, pp. 1–9, 2018.

[26] H. Sarieddeen, M.-S. Alouini, and T. Y. Al-Naffouri, "Terahertz-band ultra-massive spatial modulation MIMO," *IEEE J. Sel. Areas Commun.*, vol. 37, no. 9, pp. 2040–2052, 2019.

[27] C. Chaccour, M. N. Soorki, W. Saad, M. Bennis, P. Popovski, and M. Debbah, "Seven defining features of terahertz (THz) wireless systems: A fellowship of communication and sensing," *arXiv preprint arXiv:2102.07668*, 2021.

[28] G. Duggal, S. Vishwakarma, K. V. Mishra, and S. S. Ram, "Doppler-resilient 802.11ad-based ultrashort range automotive joint radar-communications system," *IEEE Trans. Aerosp. Electron. Syst.*, vol. 56, no. 5, pp. 4035–4048, 2020.

[29] S. H. Dokhanchi, M. R. Bhavani Shankar, K. V. Mishra, and B. Ottersten, "Multi-constraint spectral co-design for colocated MIMO radar and MIMO communications," in *IEEE International Conference on Acoustics, Speech and Signal Processing*, 2020, pp. 4567–4571.

[30] J. Liu, K. V. Mishra, and M. Saquib, "Co-designing statistical MIMO radar and in-band full-duplex multi-user MIMO communications," *arXiv preprint arXiv:2006.14774*, 2020.

[31] A. Alkhateeb, O. E. Ayach, G. Leus, and R. W. Heath, "Hybrid precoding for millimeter wave cellular systems with partial channel knowledge," in *IEEE Inf. Th. Appl. Workshop*, 2013, pp. 1–5.

[32] S. A. Busari, K. M. S. Huq, S. Mumtaz, J. Rodriguez, Y. Fang, D. C. Sicker, S. Al-Rubaye, and A. Tsourdos, "Generalized hybrid beamforming for vehicular connectivity using THz massive MIMO," *IEEE Trans. Veh. Technol.*, vol. 68, no. 9, pp. 8372–8383, 2019.

[33] H. Yuan, N. Yang, K. Yang, C. Han, and J. An, "Hybrid beamforming for terahertz multi-carrier systems over frequency selective fading," *IEEE Trans. Commun.*, vol. 68, no. 10, pp. 6186–6199, 2020.

[34] B. Ning, Z. Chen, W. Chen, Y. Du, and J. Fang, "Terahertz multi-user massive MIMO with intelligent reflecting surface: Beam training and hybrid beamforming," *IEEE Trans. Veh. Technol.*, 2021, in press.

[35] C. Lin and G. Y. L. Li, "Terahertz Communications: An Array-of-Subarrays Solution," *IEEE Commun. Mag.*, vol. 54, no. 12, pp. 124–131, Dec 2016.

[36] C. Han, J. M. Jornet, and I. Akyildiz, "Ultra-Massive MIMO Channel Modeling for Graphene-Enabled Terahertz-Band Communications," *2018 IEEE 87th Vehicular Technology Conference (VTC Spring)*, pp. 1–5, Jun 2018.

[37] X. Yu, J. Shen, J. Zhang, and K. B. Letaief, "Alternating Minimization Algorithms for Hybrid Precoding in Millimeter Wave MIMO Systems," *IEEE J. Sel. Topics Signal Process.*, vol. 10, no. 3, pp. 485–500, April 2016.

[38] Y. Xing and T. S. Rappaport, "Propagation measurement system and approach at 140 GHz - Moving to 6G and above 100 GHz," in *IEEE Global Communications Conference*, 2018, pp. 1–6.

[39] K. M. S. Huq, S. A. Busari, J. Rodriguez, V. Frascolla, W. Bazzi, and D. C. Sicker, "Terahertz-Enabled Wireless System for Beyond-5G Ultra-Fast Networks: A Brief Survey," *IEEE Network*, vol. 33, no. 4, pp. 89–95, Jul 2019.

[40] Y. Lu and L. Dai, "Reconfigurable Intelligent Surface Based Hybrid Precoding for THz Communications," *arXiv*, Dec 2020.

[41] H. Yuan, N. Yang, K. Yang, C. Han, and J. An, "Hybrid Beamforming for Terahertz Multi-Carrier Systems Over Frequency Selective Fading," *IEEE Trans. Commun.*, vol. 68, no. 10, pp. 6186–6199, Jul 2020.

[42] A. Hassanien and S. A. Vorobyov, "Phased-MIMO Radar: A Tradeoff Between Phased-Array and MIMO Radars," *IEEE Trans. Signal Process.*, vol. 58, no. 6, pp. 3137–3151, Feb 2010.

[43] N. Song, T. Yang, and H. Sun, "Overlapped Subarray Based Hybrid Beamforming for Millimeter Wave Multiuser Massive MIMO," *IEEE Signal Process. Lett.*, vol. 24, no. 5, pp. 550–554, May 2017.

[44] F. Liu, C. Masouros, A. P. Petropulu, H. Griffiths, and L. Hanzo, "Joint Radar and Communication Design: Applications, State-of-the-Art, and the Road Ahead," *IEEE Trans. Commun.*, vol. 68, no. 6, pp. 3834–3862, Jun 2020.

[45] A. M. Elbir and K. V. Mishra, "Joint antenna selection and hybrid beamformer design using unquantized and quantized deep learning networks," *IEEE Trans. Wireless Commun.*, vol. 19, no. 3, pp. 1677–1688, March 2020.

[46] A. Kaushik, J. Thompson, E. Vlachos, C. Tsinos, and S. Chatzinotas, "Dynamic RF Chain Selection for Energy Efficient and Low Complexity Hybrid Beamforming in Millimeter Wave MIMO Systems," *IEEE Trans. Green Commun. Networking*, vol. 3, no. 4, pp. 886–900, Jul 2019.

[47] T. Lin, J. Cong, Y. Zhu, J. Zhang, and K. B. Letaief, "Hybrid Beamforming for Millimeter Wave Systems Using the MMSE Criterion," *IEEE Trans. Commun.*, vol. 67, no. 5, pp. 3693–3708, Jan 2019.

[48] R. Schmidt, "Multiple emitter location and signal parameter estimation," *IEEE Trans. Antennas Propag.*, vol. 34, no. 3, pp. 276–280, 1986.

[49] A. M. Elbir, "DeepMUSIC: Multiple Signal Classification via Deep Learning," *IEEE Sensors Letters*, vol. 4, no. 4, pp. 1–4, 2020.

[50] A. M. Elbir, "A Deep Learning Framework for Hybrid Beamforming Without Instantaneous CSI Feedback," *IEEE Trans. Veh. Technol.*, pp. 1–1, 2020.

[51] F. Liu and C. Masouros, "Hybrid Beamforming with Sub-arrayed MIMO Radar: Enabling Joint Sensing and Communication at mmWave Band," *ICASSP 2019 - 2019 IEEE International Conference on Acoustics, Speech and Signal Processing (ICASSP)*, pp. 7770–7774, Dec 2017.

[52] Z. Marzi, D. Ramasamy, and U. Madhow, "Compressive Channel Estimation and Tracking for Large Arrays in mm-Wave Picocells," *IEEE J. Sel. Topics Signal Process.*, vol. 10, no. 3, pp. 514–527, April 2016.

[53] A. M. Elbir, K. V. Mishra, M. R. B. Shankar, and B. Ottersten, "A Family of Deep Learning Architectures for Channel Estimation and Hybrid Beamforming in Multi-Carrier mm-Wave Massive MIMO," *arXiv*, Dec 2019.

[54] A. M. Elbir and S. Coleri, "Federated Learning for Channel Estimation in Conventional and IRS-Assisted Massive MIMO," *arXiv preprint arXiv:2008.10846*, 2020.

[55] H. Xie, F. Gao, S. Jin, J. Fang, and Y. Liang, "Channel estimation for tdd/fdd massive mimo systems with channel covariance computing," *IEEE Trans. Wireless Commun.*, vol. 17, no. 6, pp. 4206–4218, June 2018.

[56] W. Xu, F. Gao, J. Zhang, X. Tao, and A. Alkhateeb, "Deep Learning Based Channel Covariance Matrix Estimation with User Location and Scene Images," *arXiv*, Jan 2021.

[57] N. Boumal, B. Mishra, P.-A. Absil, and R. Sepulchre, "Manopt, a Matlab Toolbox for Optimization on Manifolds," *Journal of Machine Learning Research*, vol. 15, pp. 1455–1459, 2014.

[58] S. Park, J. Park, A. Yazdan, and R. W. Heath, "Exploiting spatial channel covariance for hybrid precoding in massive MIMO systems," *IEEE Trans. Signal Process.*, vol. 65, no. 14, pp. 3818–3832, 2017.

[59] Y. Xiao, F. Norouzian, E. G. Hoare, E. Marchetti, M. Gashinova, and M. Cherniakov, "Modeling and Experiment Verification of Transmissivity of Low-THz Radar Signal Through Vehicle Infrastructure," *IEEE Sens. J.*, vol. 20, no. 15, pp. 8483–8496, Mar 2020.